

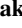


Mixing Dynamics at the Large Confluence Between the Yangtze River and Poyang Lake

Lei Xu¹ , Saiyu Yuan^{1,2} , Hongwu Tang^{1,2} , Jiajian Qiu¹ , Yang Xiao^{1,2} , Colin Whittaker³ , and Carlo Gualtieri⁴ 

¹State Key Laboratory of Hydrology-Water Resources and Hydraulic Engineering, Hohai University, Nanjing, China,

²Yangtze Institute for Conservation and Development, Nanjing, China, ³Department of Civil and Environmental Engineering, The University of Auckland, Auckland, New Zealand, ⁴Department of Structures for Engineering and Architecture, University of Napoli Federico II, Napoli, Italy

Key Points:

- Four field surveys on the mixing process downstream of a large river confluence were conducted
- Different mixing patterns were distinguished based on conductivity and hydro-acoustic measurements
- Mixing dynamics around the confluence were controlled by the momentum flux ratio, secondary flow and the lock-exchange

Correspondence to:

S. Yuan,
yuansaiyu@hhu.edu.cn

Citation:

Xu, L., Yuan, S., Tang, H., Qiu, J., Xiao, Y., Whittaker, C., & Gualtieri, C. (2022). Mixing dynamics at the large confluence between the Yangtze River and Poyang Lake. *Water Resources Research*, 58, e2022WR032195. <https://doi.org/10.1029/2022WR032195>

Received 14 FEB 2022
Accepted 17 OCT 2022

Abstract Mixing processes downstream of river confluences impacts the ecology and the related environmental management of river networks. A clear understanding of such processes is challenging, especially for confluences having width-to-depth ratios larger than 100, due to the limited available field data. In this study, four field surveys based on hydro-acoustic and conductivity measurements were conducted near the confluence between the Yangtze River and the Poyang Lake, which are the largest river and freshwater lake in China, respectively. It was found that mixing dynamics at the confluence were controlled by a complex interaction among the momentum flux ratio, secondary flow and the lock-exchange flow associated to the density contrast between the two tributaries. Slow mixing was observed during high-flow conditions that generated dual counter-rotating secondary cells, with the downwelling flow acting as a barrier in the post-confluence channel. In contrast, more rapid mixing was observed during low-flow conditions when only a single channel-scale secondary flow was identified. The mixing processes were also affected by the lock-exchange flow associated to the density difference between the two confluent flows. Such lock-exchange enhanced mixing when the Yangtze River waters had higher temperature, that is, lower density than that of the Poyang Lake. In low flow condition, the penetration of the much larger momentum flux of Yangtze River created a “two-layers” structure with the contribution of the density difference, which further enhanced the curvature-induced helicity. The findings from the present study improve our current understanding of mixing dynamics in large river confluences.

Plain Language Summary The confluence between the Yangtze River and the Poyang Lake, which are the largest river and the largest freshwater lake in China, respectively, is one of the largest on the Earth. Understanding this mixing processes at such large-scale river confluence is significantly important for local flood control and aquatic ecology management, but even challenging due to the lack of detailed field data. Four field surveys were conducted to investigate hydrodynamics, water quality and mixing at the confluence of the Yangtze River and Poyang Lake. The effect of momentum and density difference between the two rivers and large-scale secondary flow on mixing processes was identified. The results of the present study indicated that such density difference can produce different patterns of vertical stratification which are related to the mixing between the Yangtze River and the Poyang Lake.

1. Introduction

Confluences are locations where flows from different tributaries converge, resulting in mixing in the post-confluence channel. Complete transverse mixing between the two streams can occur over the mixing interface over a distance when two streams that have significantly different sediment loads, temperatures, or dissolved chemical and nutrient loads confluence (Gaudet & Roy, 1995; Lewis et al., 2020; Lewis & Rhoads, 2015). The mixing distance scales with the product of the post-confluence channel width by its aspect ratio (Rutherford, 1994). Thus, mixing at river confluences may occur over very long distances, especially for large rivers. This requirement is confirmed in many cases by aerial field measurements and satellite observations (Bouchez et al., 2010; Rathbun & Rostad, 2004; Stallard, 1987; Umar et al., 2018). However, in some other cases mixing could be strongly influenced by the complex flow structure within the confluence hydrodynamic zone (CHZ), and consequently occur over very different length scales (Kenworthy & Rhoads, 1995; Lane et al., 2008; Pouchoulin et al., 2020). This study focuses on the mixing dynamics within the CHZ of river confluences.

© 2022. The Authors.

This is an open access article under the terms of the [Creative Commons Attribution-NonCommercial-NoDerivs License](https://creativecommons.org/licenses/by-nc-nd/4.0/), which permits use and distribution in any medium, provided the original work is properly cited, the use is non-commercial and no modifications or adaptations are made.

According to the width-to-depth ratio, confluence scales could be classified as small ($W/H < 10$), medium ($10 < W/H < 50$), and large scale ($W/H > 50$), as suggested by Yuan et al. (2021). Research on confluence hydrodynamics at various scales is crucial for the scaling-up of river processes to the drainage network scale. The CHZ generally includes a zone of flow stagnation near the upstream junction corner, an area of flow deflection as the tributary enters the confluence, a shear layer and/or mixing interface between the two converging flows, a possible separation zone at the downstream junction corner, flow acceleration within the post-confluence channel, and flow recovery at the downstream end of the CHZ (Best, 1987; Bradbrook et al., 2000; Weber et al., 2001; Yuan, Xu, Tang, Xiao, & Gualtieri, 2022). Such flow structure, as well as sediment transport and morphodynamics, have been extensively studied (Best, 1987; Guillén-Ludeña et al., 2016, 2017; Herrero et al., 2016; Leite Ribeiro et al., 2012; Li et al., 2022; Rhoads & Kenworthy, 1995; Roy & Bergeron, 1990; Gualtieri et al., 2018; Ianniruberto et al., 2018; Sukhodolov & Sukhodolova, 2019; Yuan et al., 2016, 2018, 2021; Yuan, Zhu, et al., 2022). However, scale effects cannot be ignored when applying conceptual models developed for small-scale confluences to the larger-scale confluences that drain large basins. Compared to small-scale confluences, such large-scale confluences are likely to have a broader range of inflow conditions in terms of their water chemistry, sediment concentration, and densities (Gualtieri et al., 2019; Lane et al., 2008). Understanding the hydrodynamics and mixing processes at large-scale confluences is vital in efforts to control and regulate water with the broader goal of enhancing the ecological quality of the aquatic environment (Yuan, Xu, Tang, Xiao, & Whittaker, 2022). However, few field studies have examined the influence of the buoyancy and inertial effects on mixing dynamics at large-scale confluences (Lane et al., 2008 in the Paranà River; Gualtieri et al., 2019 in the Amazon River).

Mixing rates generally depends on the combined effects of molecular diffusion which is usually negligible, turbulent diffusion and lateral dispersion (Rutherford, 1994). Mixing is due first to the shear between the two incoming flows, characterized by turbulent eddies that develop at the mixing layer scale (Biron et al., 2019) and substantially enhance transverse mixing in the near-field region downstream of the confluence. In addition to shear dispersion, mixing may be enhanced by convective effects due to large-scale, persistent flow structures, often helical in shape. Helical motions generate lateral and vertical velocity components that can be observed in a meander bend (Best, 1988; Constantinescu et al., 2016; Mosley, 1976; Rhoads & Kenworthy, 1995, 1998; Rhoads & Sukhodolov, 2001); these have been shown to have a strong effect on mixing at a confluence (Lewis & Rhoads, 2015; Rhoads, 1996; Rhoads & Kenworthy, 1995; Rhoads & Sukhodolov, 2001). The dynamics of secondary circulation at river confluences have also received considerable attention. Secondary circulation cells are influenced by the momentum flux ratio between the two flows and the bed geometry (Best, 1988; Cheng & Constantinescu, 2020; Mosley, 1976; Sukhodolov & Sukhodolova, 2019). At large river confluences, empirical evidence and theoretical analysis suggest that the high width-to-depth ratio in wide rivers may impede the formation of coherent channel-size secondary flow cells (McLelland et al., 1996, 1999; Parsons et al., 2007). For example, at the large braid-bar confluences at Paranà River, the helical motion was restricted in the spatial extent to portions of the flow near the mixing interface (Szupiany et al., 2009), or even these channel-scale secondary circulation cells were absent (Parsons et al., 2007). They attributed this to the large channel width-to-depth ratio that allowed the effects of form roughness to become dominant, but the effects may be localized and not extend across the entire channel width. In the large river confluence between the Paranà and Paraguay Rivers, it was observed that the mixing length between the confluent flows was related to the presence or absence of a channel-scale circulation pattern (Lane et al., 2008). Such channel-scale circulation is generally controlled by the interaction between bed discordance, downstream topographic forcing, density effect and the momentum ratio between the confluent channels. Therefore, the factors that initiate and enhance (or inhibit) helical motions are still not fully understood at the large river confluences.

Previous studies have demonstrated that density differences play an important role on confluence hydrodynamics and mixing if such differences produce buoyant forces comparable to inertial forces as indicated by the densimetric Froude number (Fr_d) (Cheng & Constantinescu, 2018, 2020; Gualtieri et al., 2019; Herrero et al., 2018; Jiang et al., 2022; Laraque et al., 2009; Lewis & Rhoads, 2015; Lyubimova et al., 2014; Prats et al., 2010; Ramón et al., 2014, 2016). Underflows of denser water beneath less dense water have been documented at some large river confluences (Herrero et al., 2018; Lane et al., 2008; Laraque et al., 2009). Those buoyant forces might reinforce or weaken secondary motions associated with helical motion if the tributary waters have a density lower or higher density than that of main channel waters, respectively (Horna-Munoz et al., 2020; Ramón et al., 2013). However, studies on how density differences affect confluence flows, such as the development of the mixing

interface (Rhoads & Sukhodolov, 2004), or helical motions induced by flow curvature (Ashmore et al., 1992; De Serres et al., 1999; Lewis & Rhoads, 2015; Paola, 1997; Rhoads, 1996; Rhoads & Sukhodolov, 2001), have received limited attention in published field studies (e.g., Lewis & Rhoads, 2015; Lewis et al., 2020; Duguay et al., 2022a; Rhoads & Johnson, 2018).

The present field study was undertaken to investigate hydrodynamics and mixing dynamics at a large confluence between the Yangtze River and the outflow channel of Poyang Lake. They are the largest river and the largest freshwater lake in China, respectively, and have significant density differences. Both have a dramatic influence on flood flows, water resources management, water chemistry as well as environmental and ecological protection within the Yangtze River basin. In the confluence reach, the Yangtze River has an average width of almost 2 km. The main goals of the present field study on such a large-scale, asymmetrical and concordant bed confluence are to investigate (a) the mixing patterns in the post-confluence channel; (b) how any change in the inflow conditions affects both hydrodynamics and mixing processes within the CHZ; and (c) how density differences between the incoming flows impact on confluence hydrodynamics, like the large-scale helical motions observed by Yuan et al. (2021). These results can improve our current understanding of and ability to predict watershed-scale pollutant transport and its ecological impacts.

2. Study Site, Field Procedures, and Methods

2.1. Study Site

The Yangtze River catchment is one of the largest drainage basins in the world; its annual water discharge ($9,000 \times 10^8 \text{ m}^3/\text{yr}$) and sediment load ($4.78 \times 10^8 \text{ t/yr}$) are ranked as the fifth and fourth largest in the world, respectively. The confluence of the Yangtze River and Poyang Lake is located about 900 km downstream the Three Gorges Dam (TGD) and 800 km upstream of the Yangtze River estuary (Figure 1a). The Poyang Lake watershed plays an important role in flood-mitigation storage and the protection of biodiversity. It is located at the junction of the south bank of the Yangtze River (Figure 1a), with an area of 162,200 km² covering 9% of the Yangtze River basin. The confluence is a key node for the exchange of water, sediment and pollutants between the Yangtze River and Poyang Lake. In summer, when the water level of the Yangtze River is higher than that of Poyang Lake, the backwater effect of Yangtze River on Poyang Lake affects lacustrine water chemistry. Moreover, previous research suggests that the TGD operation has affected the Yangtze River discharge and water level, ultimately altering the interaction between that river and the Poyang Lake. This in turn creates severe and extended dry seasons in the Poyang Lake (Guo et al., 2012).

For the 2020–2021 years (Figure 2), the average discharge in the Yangtze River and the Poyang Lake was 27227.9 and 4995.2 m³/s, respectively, which is close to the average annual flood of 30,146 and 4,836 m³/s for the Yangtze River and the Poyang Lake, respectively. Near Jiujiang Station, Zhangjia Island divides the Yangtze River flow into two parts (each flow having ~ 50% total discharge) which meet about 19 km downstream from Jiujiang Station with an angle of convergence nearing 90° (Figure 1b), that is, the branch at the left of this island also belongs to the Yangtze River. In this study, the Yangtze River mentioned hereafter means the branch at the right of the Zhangjia Island. The confluence of the Yangtze River and the Poyang Lake has an angle of about 58° and its apex is located at the Meijia Island. The discharge of branch between the Unnamed Inland and Zhangjia Island is very small, accounted for less than 5% of the discharge of the receive channel. In addition, the branch was located in the left bank of the receiving channel, and it is expected to have negligible effect on the mixing dynamics. Therefore, it was not considered in this study. Due to the large area covered and the shallow depth, the water temperature of Poyang Lake is higher in summer and lower in winter than that of the Yangtze River, with a temperature difference of about 1.5–3°C. In addition, at the confluence, water conductivity in the Yangtze River (average value = 320 μS/cm among the four surveys) is generally larger than that in the Poyang Lake (average value = 141 μS/cm among the four surveys), also contributing to a difference in water density between the tributaries.

2.2. Instrumentation and Field Procedures

Four field surveys were carried out at this confluence during the years 2020 and 2021. According to the discharge sequences of Yangtze River in Figure 2, Survey 1 (August 2020) and Survey 4 (June 2021) were both carried out in high-flow conditions (defined as the discharge of Yangtze River >30,000 m³/s), after and before flood in

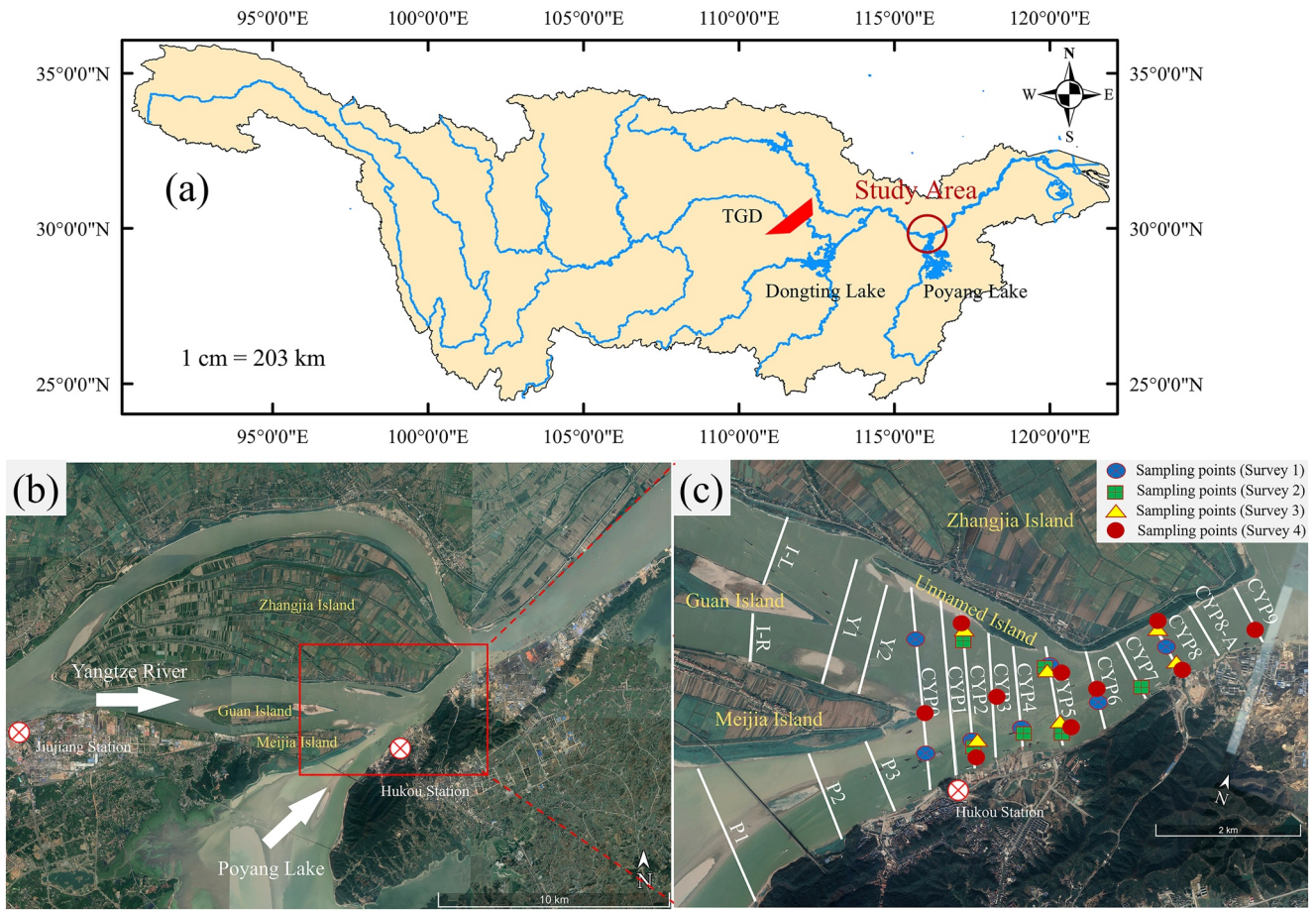


Figure 1. (a) Map of the Yangtze River basin shows that the confluence of the Yangtze River and the Poyang Lake is in the middle and lower reach of the Yangtze River (near 29.75°N, 116.22°E); (b) locations of hydrological stations and islands; (c) map of measurements locations at the confluence during four surveys: The white lines mark cross sections for ADCP measurement, while the symbols indicate water chemistry sampling points.

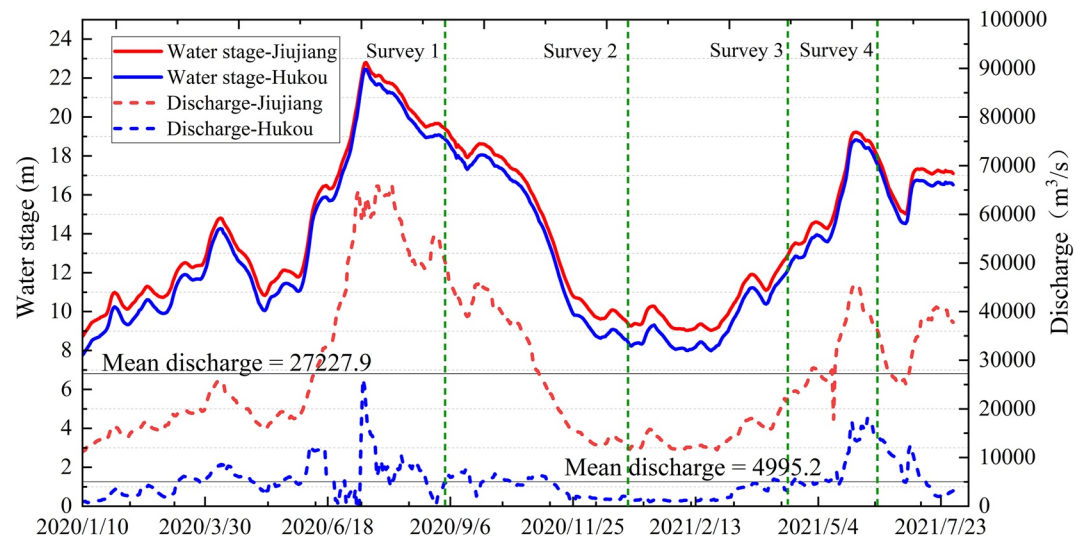


Figure 2. Annual variation of water level and flow discharge at Jiujiang and Hukou stations (Figure 1b). The water level is based on the frozen base level whose zero datum is 1.91 m higher than that of 1,985 National Height Datum.

the Yangtze River, respectively. Survey 2 (December 2020) was conducted during a low flow condition (defined as the discharge of Yangtze River $<20,000 \text{ m}^3/\text{s}$), while Survey 3 was carried out in April 2021 in medium flow condition (defined as the discharge of Yangtze River was $20,000 \sim 30,000 \text{ m}^3/\text{s}$) when the floodplain at the outflow of the Poyang Lake was just submerged.

A total of 18 and 17 locations were considered in the two tributaries and the post confluence during Surveys 1, 2, 4 and during Survey 3 (CYP8 and CYP8-A were merged into CYP8 which was in the middle of the two cross sections), respectively. These transects correspond to those previously considered by Yuan et al. (2021). In the present study, the transects in the post confluence channel were considered to analyze the mixing dynamics. Two acoustic Doppler current profiles (ADCPs), namely a Sontek River Surveyor M9 Instrument and a Rio Grande 600 kHz RDI Instrument, were used simultaneously. The two ADCPs were used at the same time to ensure that the flow discharge difference of a series of three repeat transects measured by the two instruments was within 3% in each transect (Rhoads & Johnson, 2018). The 600-kHz Workhorse Rio Grande ADCP was configured for a sampling rate of 1 Hz, bin size of 0.50 m, blanking distance of 0.25 m, Water Mode 1, and Bottom Mode 5. These parameters were selected based on the default manufacture recommendations and previous studies for large rivers (Teledyne RD Instruments [TRDI], 2013; Jamieson et al., 2011; Rennie & Church, 2010). The ADCP M9 is a double frequency instrument, with four transducers at both 1 and 3 MHz. The frequency and thus cell sizes are changed automatically on-the-fly depending on the local water depth, if not configured otherwise (SonTek, 2012). Along the confluence cross-sections, the shallow margins were usually sampled at a frequency of 3 MHz, and the deeper channel at a frequency of 1 MHz, both in Narrowband mode. The vertical size of the measurement cells ranged 0.1–0.5 m for the 3 MHz and 0.5–2.0 m for the 1 MHz. The horizontal sampling size is determined as a function of the boat's movement in time, and the data acquisition frequency ($f = 1 \text{ Hz}$). The ADCPs provided three-dimensional flow velocities in each cross-section. In this study, the velocity data from the M9 were processed to analyze the flow structure. As the Sontek M9 firmware changes the acoustic operating frequency depending on the water depth and velocity (smart pulse) and only provide SNR (Signal to Noise Ratio), therefore the data from RDI were not only used to verify the discharge accuracy but also to provide the information about acoustic backscatter intensity which is related to suspended sediment concentration. As the surveys we being undertaken using a moving vessel, these raw velocities then must be corrected again for the boat velocity. There are two key methods for doing this. The first uses the bottom tracking to measure the boat velocity relative to the riverbed, under the assumption that the latter is stationary (i.e., there is no bedload transport). The second tracks the boat position using differential global positioning system (DGPS) (e.g., Zhao et al., 2014). In this study, boat position and velocity were determined using a DGPS receiver. The bottom tracking function of the ADCPs was not used due to the measurement errors that bed load transport can introduce into the results obtained (Rennie & Church, 2010; Szupiany et al., 2009). In addition, the data obtained by the ADCPs were corrected by adjusting the GC-BC (angle of average GPS course since start of transect minus ADP bottom-track course; value near 0 is desired) $<2^\circ$ and D (BT)/D(GPS) (Ratio of Bottom Track distance to GPS track distance) approximately 1 (SonTek, 2012). The DGPS-antenna was affixed to the port side mount directly above the ADCP. The DGPS-receiver provides time-stamped geographic coordinates at 10 Hz with up to sub-meter accuracy and was integrated with the ADCP to fully geo-reference velocity data at each ensemble. The compass was well calibrated, the boat velocity and track position of the survey lines were monitored online by the helmsman and were held constant as much as possible during the surveys. Due to the extremely harsh sampling conditions, for example, large-scale channel width and the large number of ships navigating in the area, a constant boat speed of approximately 2 m/s was used while collecting these transects where the flow velocities was quite high to ensure minimal lateral variations about the line, as well as to decrease the number of missing ensembles. The boat speed/river velocity ratio was about 0.8. To ensure that every ADCP measured velocity vectors are in the right direction, calibration tests were made for the inner compass of each device (heading, pitch, and roll).

Furthermore, during all the campaigns, local conductivity was measured over the water depth at 7 sampling points in Survey 1, 6 sampling points in Surveys 2 and 3, and 10 sampling points in Survey 4 (Figure 1c) using an YSI EXO2 multi-parameter probe (EXO2 probe). Considering the density effects at this confluence, the sampling frequency of EXO2 probe was set as 1 Hz. It can generate time/depth series of water quality parameters in the vertical direction of each sampling point to continuously capture the water quality data. According to the manufacturer's specifications, the probes have a 0.04 m accuracy on the water depth measurements and 1% accuracy on the electrical conductivity measurement. At the same time, the total suspended sediment (TSS) concentrations were measured using the water sampling (Figure 1c). Depending on the water depth, three different depth samples

in one vertical were collected. The EXO2 probe was also deployed at the edge of the vessel together with ADCP and provided the longitude and latitude information through the built-in GPS in the handheld device. The sensors of the EXO2 probe were 0.6 m below the water surface, and a section was set every 100 m in the study area to derive the distribution of surface water chemistry parameters. Before each measurement, the sensors were tested using the manufacturer's specifications for continuous water-chemistry monitoring.

2.3. Data Post-Processing

RDI data and M9 data were exported as ASCII files and MATLAB files using Teledyne RDI WinRiverII software and RiverSurveyor Live software, respectively. The data for multiple transects were then analyzed using the velocity mapping tool (VMT), a suite of MATLAB routines with a graphical user interface (Parsons et al., 2013). VMT composites and averages ADCP velocity data from repeat transects along cross-sections, providing the capability to plot 3-D velocity vectors. In this study, the instantaneous velocity data from the M9 were averaged between a series of three repeated-transect lines and processed to analyze the flow structure, while the data from RDI were used mainly to verify their discharge accuracy during the field surveys and provide the information about acoustic backscatter intensity to analyze the mixing processes. The M9 and RDI data were smoothed using the VMT beforehand by adjusting the grid node spacing, horizontal/vertical vector spacing, and horizontal/vertical smoothing window.

In confluences field studies, it is commonly difficult to keep the transects orthogonal to the flow direction, especially at a high confluence angle. Some methods (e.g., Lane et al., 2000) can be used to minimize the secondary circulation in the transect but it is needed to know what the minimum secondary circulation transect path is, which is difficult to know a priori. Thus, in this study, the transects were chosen to be orthogonal to the stream path of the CHZ as much as possible to capture the mixing processes and the helical motions more accurately. The identification of helical motion at confluences based on patterns of secondary flow is sensitive to the frame of reference used to represent this flow (Lane et al., 2000; Rhoads & Kenworthy, 1998, 1999). The present study adopted the Rozovskii definition which had been used in the same site by Yuan et al. (2021) to calculate and plot the primary and secondary velocity. The Rozovskii reference frame rotated each vertical ensemble of velocity measurements such that primary and secondary velocity components are aligned parallel and perpendicular to the orientation of the depth-averaged velocity vector, respectively. This method was found useful to identify helical motion in strongly converging flows (Rhoads & Kenworthy, 1998; Rozovskii, 1954, 1957; Szupiany et al., 2009; Yuan et al., 2021).

Confluence bathymetry and distribution of water chemistry parameters on the surface in each survey were prepared using a continuous recording of depth values using the ADCP and water chemistry parameters along the planned trajectory. These depth values and water chemistry parameters were then interpolated on a grid covering the area of interest, using a kriging procedure which is widely used in geostatistics (Gualtieri et al., 2017; Herrero et al., 2018; Yuan et al., 2021).

Water density was calculated from the measured water temperature and then adjusted to consider the contribution from the TSS concentration and specific conductivity (Ford & Johnson, 1983; Gualtieri et al., 2019; Ramòn et al., 2013; Moreira et al., 2016). The following equations were applied:

$$\rho \approx \rho_{\lambda}(T, k_{25}) = \rho_w(T) + k_{25}[\lambda_0 + \lambda_1 \times (T - 25^{\circ}\text{C})] \quad (1)$$

$$k_{25} = \frac{k}{1 + 0.0191(T - 25^{\circ}\text{C})} \quad (2)$$

$$\Delta\rho_{\text{TSS}} = \text{TSS} \left(1 - \frac{1}{\text{SG}}\right) 10^{-3} \quad (3)$$

where ρ_w is the density of pure water, which can be accurately calculated (Kell, 1975). k is specific conductivity (k_{25} is conductivity at 25°C, $\mu\text{S cm}^{-1}$), λ_0 and λ_1 are coefficients correlated with temperature and k_{25} , which can be obtained by the RHO_LAMBDA approach (Moreira et al., 2016). $\Delta\rho_{\text{TSS}}$ represents the density difference caused by different suspended sediment concentrations. SG is the specific gravity of suspended solids, assumed equal to 2.65.

Table 1
Main Flow Properties and Water Chemistry Characteristics of Yangtze River and Poyang Lake

Date of the survey		23 August 2020: Survey 1	21 December 2020: Survey 2	16 April 2021: Survey 3	01 June 2021: Survey 4
Yangtze River (Main channel, measured in Y2)	Temperature T_{main} (°C)	28.3	11.5	16.7	22.3
	Conductivity (μS/cm)	315.9	342.6	342.7	277.9
	TSS (mg/L)	59.3	32.4	45.3	28.6
	Density ρ_{main} (kg/m ³)	996.4	999.8	999.1	997.9
	Wetted area A (m ²)	29,721	8,266	15,414	26,273
	Discharge Q_{main} (m ³ /s)	24,573	7,633	13,549	20,838
	U_{main} (m/s)	1.03	0.92	0.99	0.83
Poyang Lake (Tributary; measured in P3)	Temperature T_{trib} (°C)	30.6	8.6	18.0	24.9
	Conductivity (μS/cm)	84.1	220.8	150.5	109.4
	TSS (mg/L)	7.8	25.5	29.1	21.1
	Density ρ_{trib} (kg/m ³)	995.5	1,000.0	998.7	997.1
	Wetted area A (m ²)	17,041	4,975	8,782	15,082
	Discharge Q_{trib} (m ³ /s)	9,028	1,440	5,031	17,550
	U_{trib} (m/s)	0.47	0.29	0.62	1.18
Confluence (CYP1)	U (m/s)	0.84	0.62	0.80	0.99
	Width b (m)	2488	2041	2170	2422
	Mean depth H (m)	17.35	6.32	12.75	16.27
	Water level (m)	18.94	9.09	12.52	18.69
	Momentum flux ratio M_r	0.17	0.06	0.23	1.19
	Discharge ratio Q_r	0.37	0.19	0.37	0.83
	Velocity ratio V_r	0.45	0.31	0.63	1.43
	$\Delta\rho$ (kg/m ³)	$\overline{0.9}$	$\overline{-0.2}$	$\overline{0.4}$	$\overline{0.8}$
	$\Delta\rho/\rho_0 \times 10^{-4}$	8.4	-1.7	3.6	7.4
	Fr_d	2.2	6.2	2.9	2.9

Note. TSS = total suspended sediments; U = average cross-sectional velocity (measured using the ADCP); ρ = water density (calculated using Equations 1–3) and ρ_0 is ρ_{main} . $\Delta\rho = \rho_{\text{main}} - \rho_{\text{trib}}$. $M_r = \rho_{\text{trib}} Q_{\text{trib}} U_{\text{trib}} / (\rho_{\text{main}} Q_{\text{main}} U_{\text{main}})$, $Q_r = Q_{\text{trib}} / Q_{\text{main}}$, $V_r = U_{\text{trib}} / U_{\text{main}}$, and $\Delta\rho/\rho_0 = (\rho_{\text{main}} - \rho_{\text{trib}}) / \rho_{\text{main}}$. $Fr_d = U / \sqrt{|\Delta\rho/\rho_0| g H}$, where U and H are defined as average velocity and cross-sectional depth at the transect CYP1, respectively. The water level values were provided by the Hukou hydrologic station.

3. Results and Discussion

3.1. Hydraulic and Density Conditions

Table 1 lists the hydraulic parameters of the Yangtze River and Poyang Lake calculated from the ADCP measurements during the four surveys. Surveys 1 and 3 have similar discharge ratios ($Q_r \sim 0.37$; the parameters Q_r , M_r , etc. are introduced at Table 1.) and momentum flux ratios ($M_r \sim 0.2$). Despite the discharge of Poyang Lake in Survey 1 being nearly twice that in Survey 3, the average velocity in the outflow channel was lower in Survey 1 than in Survey 3. This may be due to the Yangtze River's increased backwater effects in August leading to a more than doubled wetted area in the Poyang Lake and to a lower velocity. It is worth noting that in Survey 4 momentum flux ratio ($M_r = 1.19$) was close to 1, suggesting that the wake mode within the mixing interface may play an important role in CHZ. The largest differences in discharge and flow velocities were observed in Survey 2, leading to a substantially lower momentum flux ratio ($M_r = 0.06$) than in the other surveys.

Table 1 also lists the water chemistry characteristics, and the relative density difference $\Delta\rho$ observed during the field surveys. A notation is adopted to convey both the magnitude and direction of $\Delta\rho$ (Duguay et al., 2022b). In Survey 1, the Yangtze River was estimated to be 0.9 kg/m³ denser than the Poyang Lake and because the Yangtze River is the left tributary, density decreased across the mixing interface from left to right. We denoted this as $\overline{\Delta\rho}$ with the arrow pointing in the lateral direction of decreasing density. Temperature, water conductivity, and TSS

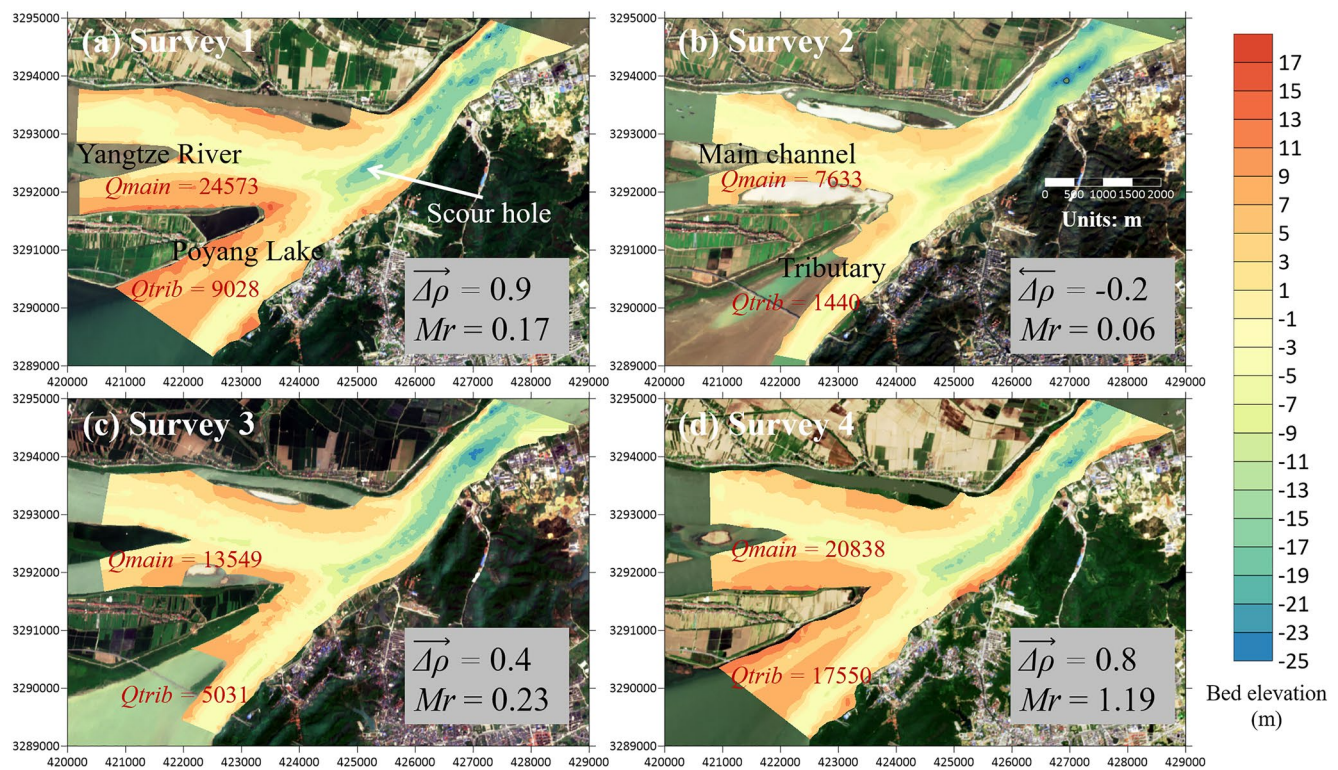


Figure 3. Bed elevations of the confluence during the field surveys. Bed elevations were calculated by the minus of the water level at Hukou Station and the water depth of the whole study site measured by ADCP. Q_{main} and Q_{trib} are the discharge (m^3/s) in the Yangtze River and Poyang Lake outflow, respectively. The values of $\Delta\rho$ (with an arrow to indicate the direction of decreasing density gradient), and M_r were consistent with Table 1. Background images were obtained by using remote sensing (Sentinel-1/2 with low cloud cover conditions $<10\%$) during each survey.

showed significant differences between the two incoming flows; hence they were applied to quantify the density difference. The water temperature in the Yangtze River was about $2.5^\circ C$ lower than that in Poyang Lake in Survey 1, 3 and 4, while it was the opposite in Survey 2. This could be explained considering that the temperature of Poyang Lake with a large surface area could be significantly affected by the solar irradiance and ambient air temperature. A large difference in water conductivity was found between the two tributaries. In addition, as water supply in the Poyang Lake region is primarily derived from groundwater during the dry season (Bing, 2018; Xu et al., 2021), the conductivity of Poyang Lake in Survey 2 was nearly three times that in Survey 1 (Table 1). TSS concentration in the Yangtze River showed a positive correlation with its average velocity (U_{main}). Interestingly, TSS concentration of Poyang Lake was only 7.8 mg/L in Survey 1, a much lower value than in other surveys (in average 25.2 mg/L). This may be due to the stronger backwater effect of the Yangtze River on the outflow of Poyang Lake (Fang et al., 2012).

The observed temperature, conductivity and TSS data were then used to calculate the water density in each tributary according to Equations 1–3. Previous literature (Gualtieri et al., 2019; Herrero et al., 2018; Horna-Munoz et al., 2020; Lewis & Rhoads, 2015; Lyubimova et al., 2014; Pouchoulin et al., 2020; Ramón et al., 2013, 2014) suggested that hydrodynamics and mixing processes are affected by density difference if $Fr_d < 5$. In the present study, Fr_d was in the range from 2.2 to 2.9 in Surveys 1, 3 and 4, while it was >5 in Survey 2 ($Fr_d = 6.2$) (Table 1). Therefore, it is expected that the buoyant forces cannot be ignored in all our field surveys, but in Survey 2 their effect should be limited and different because in Surveys 1, 3 and 4, Yangtze River waters were denser, while the opposite was in Survey 2.

3.2. Bed Morphology Features

Figure 3 shows confluence bed elevations obtained by interpolating the values of water level minus the water depth collected with ADCP in the present surveys. Surveys 1 and 2 have maximum and minimum water depths,

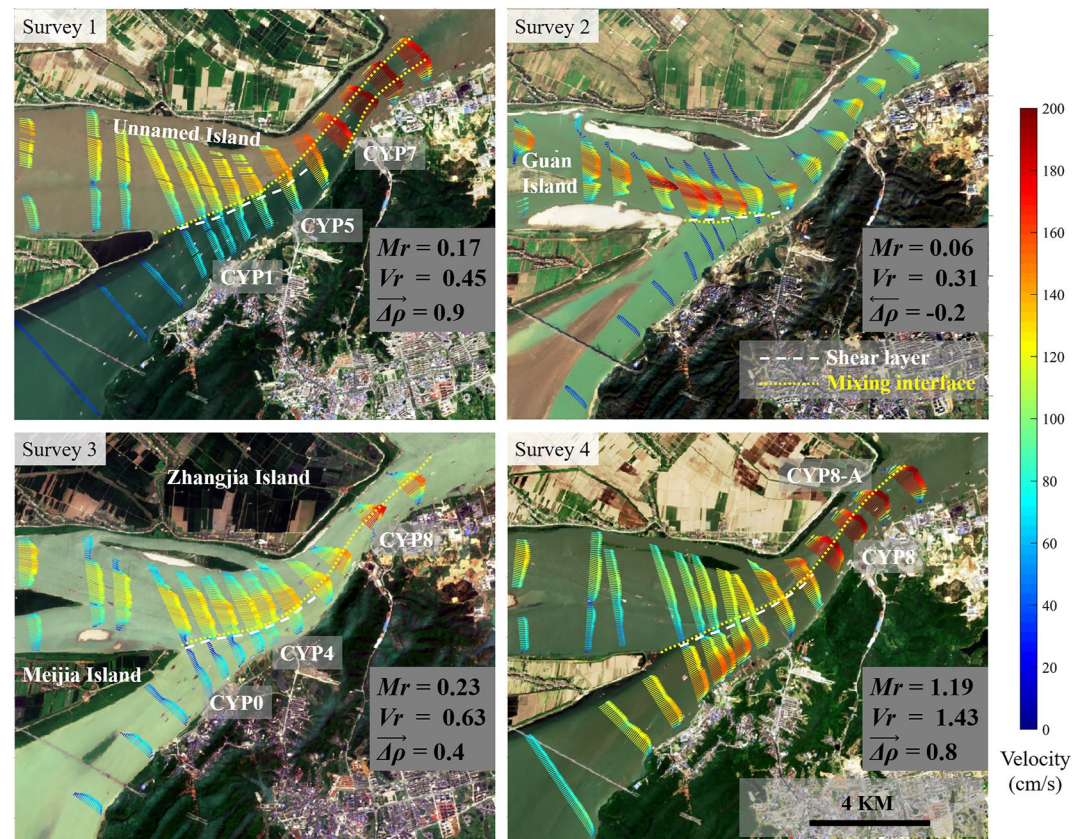


Figure 4. Map with depth-averaged velocities during the four surveys. Note that the shear layer was identified using the depth-averaged velocity, while the mixing interface data were gained from the surface water conductivity. Background images were obtained by using remote sensing (Sentinel-1/2 with low cloud cover conditions <10%) during each survey. The values of $\Delta\rho$ (with an arrow to indicate the direction of decreasing density gradient), V_r and M_r were consistent with Table 1.

respectively, among the four surveys (Table 1). The thalweg of the two tributaries shows that the confluence, studied here, has relatively concordant beds and an asymmetric planform with an angle of 58° . Thus, the bed discordant effect on secondary flow and mixing, mentioned in the previous literature studies (e.g., Biron, Best, et al., 1996; Biron, Roy, et al., 1996; Biron et al., 1999; Sukhodolov et al., 2017), was not relevant. In addition, because the discharge ratios were less than 1, the thalwegs were located on the right bank of the post-confluence channel. The scour hole observed in Surveys 1, 3, and 4 was stretched to form a deep channel in Survey 2, which is consistent with previous studies (Yuan et al., 2021). In addition, acceleration of flow through the deep channel may strengthen curvature-induced helicity during low flow condition (Lewis et al., 2020).

3.3. Depth-Averaged Flow Field and Three-Dimensional Flow Field

Figure 4 shows the depth-averaged velocity collected at each transect in the field surveys and remote sensing images during each survey. In medium and high flow conditions (Surveys 1, 3, and 4), the floodplains on the right side of the Yangtze River and on the left side of the Poyang Lake were submerged. Near the junction apex between the Yangtze River and the Poyang Lake outflow channel, a stagnation zone whose size and location changed under the different flow conditions was observed. Previous studies indicated that the development of large stagnation zones is often associated with M_r and V_r close to 1 (Constantinescu et al., 2011). Although both parameters were close to 1 in Survey 4 ($M_r = 1.19$), the corresponding size of the stagnation zone was lower than that in Survey 3 ($M_r = 0.23$). This is probably related to the low-velocity flow in the submerged floodplain which reduced the lateral shear between the tributaries and affected the development of the stagnation zone. The location of the shear layer is defined by the strong velocity gradient between the two flows. As the Yangtze River and Poyang Lake entered the confluence, the channel width was almost 3 km, with the two waters merging about

a strong and easily visible shear layer. In Surveys 1 and 3, the shear layer tended to the right bank due to the larger momentum flux on the Yangtze River side. However, in Survey 4 ($M_r = 1.19$), Poyang Lake flow pushed the shear layer position toward the center of the post-confluence channel. Flow deflection is commonly observed at river confluences, as indicated by the change in direction of the velocity vectors of the converging flows in the post-confluence-channel. During Surveys 1, 3, and 4, complete re-alignment of the Poyang Lake flow to with the Yangtze River post-confluence channel occurred at about CYP7, which was located 3 km downstream of the junction apex.

During Survey 2 ($M_r = 0.06$), complete re-alignment of the Poyang Lake flow to the Yangtze River post-confluence channel occurred at about CYP6, which was located about 2.4 km downstream of the junction apex, while a significant separation zone was not observed. However, near the junction apex low flow velocities toward upstream were observed upstream of the shear layer, due to the backwater effect into the Poyang Lake whose discharge was too small to affect the Yangtze flow direction. The confluent flows swerved from CYP4 to CYP6 with an anti-clockwise angle of nearly 39° , mainly affected by the bend topography. Similarly, between CYP8 and CYP9, the direction of the flow velocity once again produced a clockwise change, which was consistent with the change of the thalweg in Figure 3b.

Figures 5a–5d show the vectors of the secondary current velocity superimposed on the contours of the primary flow velocity using the Rozovskii definition during the medium and high flow conditions (Surveys 1, 3, and 4). There were dual counter-rotating cells in the near-field cross-sections from CYP2 to CYP6 in all surveys. The left helical cell at the Yangtze side was generated by the Yangtze flow curvature, whose strength depended mainly on the flow curvature, and on M_r (Constantinescu et al., 2011; Yuan et al., 2021). This helical cell got stronger in Survey 4 due to a larger force from the Poyang Lake, corresponding to the large momentum ratio ($M_r = 1.19$). An anti-clockwise helical cell was observed on the right side near CYP2 for all the surveys. Since the secondary flow velocity has the same order of magnitude as the primary flow velocity, the helical cell cannot be attributed solely to the curvature of the Poyang Lake flow. Additional factors like the penetration of the near-bed Yangtze flow (as suggested by Yuan et al., 2021), which had a larger density ($Fr_d < 3$) and momentum flux into the Poyang flow cannot be discounted. Downstream of CYP2, the outflow of Poyang Lake was deflected clockwise owing to the squeezing of the flow by the Yangtze River (Figure 4). This, combined with the impact of the flow penetration, resulted in a considerable rise in the secondary flow velocity. It is worth noting that Survey 1 was dominated by a large-scale counter-clockwise helical cell after CYP6, but there were always dual counter-rotating cells in Surveys 3 and 4 till CYP8. This may be the result of the combined effect of relative density difference and momentum ratio. This will be discussed later.

Figure 5b shows the vectors of the secondary velocity superimposed on the contours of the primary velocities under low flow condition (Survey 2). Compared with Surveys 1, 3, and 4, the velocity in the Poyang Lake outflow channel was much smaller. Due to the minor density difference between the tributaries ($Fr_d = 6.2$), helical cells caused by flow penetration were not observed at two sides of the shear layer at CYP2. While a single, channel-scale, clockwise secondary circulation occurred and developed from CYP4 to CYP8, whose size gradually decreased downstream, that is, the size of the secondary circulation had its maximum at CYP4. Interestingly, Yuan et al. (2021) reported that in December 2018 the size of the channel-scale helical cell had its maximum at CYP5 and CYP6, where the bend curvature was the largest. That difference may be related to the stratification observed during the present study in CYP4 caused by momentum flux and density contrast. The fast homogenization of velocity in Survey 2 ($M_r = 0.06$) (Figure 4b) was likely related to such channel scale helical cell resulting a strengthened exchange of the lateral momentum (Lewis & Rhoads, 2015).

3.4. Mixing Patterns

Water conductivity was a suitable tracer to illustrate the mixing processes at the confluence of the Yangtze River and the Poyang Lake, which naturally have a large difference in water conductivity. Moreover, water conductivity is a conservative parameter (Gaspar, 1987) and can be continuously recorded in situ using multiparameter water chemistry meter, as suggested by Moody (1995) and Pouchoulin et al. (2020).

Figure 6 shows the contours of conductivity ($\mu\text{S}/\text{cm}$) near water surface at the confluence during the four field surveys. For the medium and high flow conditions (Figures 3a–3d), the maps of conductivity highlighted slow mixing processes with clear mixing interfaces near the water surface, maintained for a long distance. It is

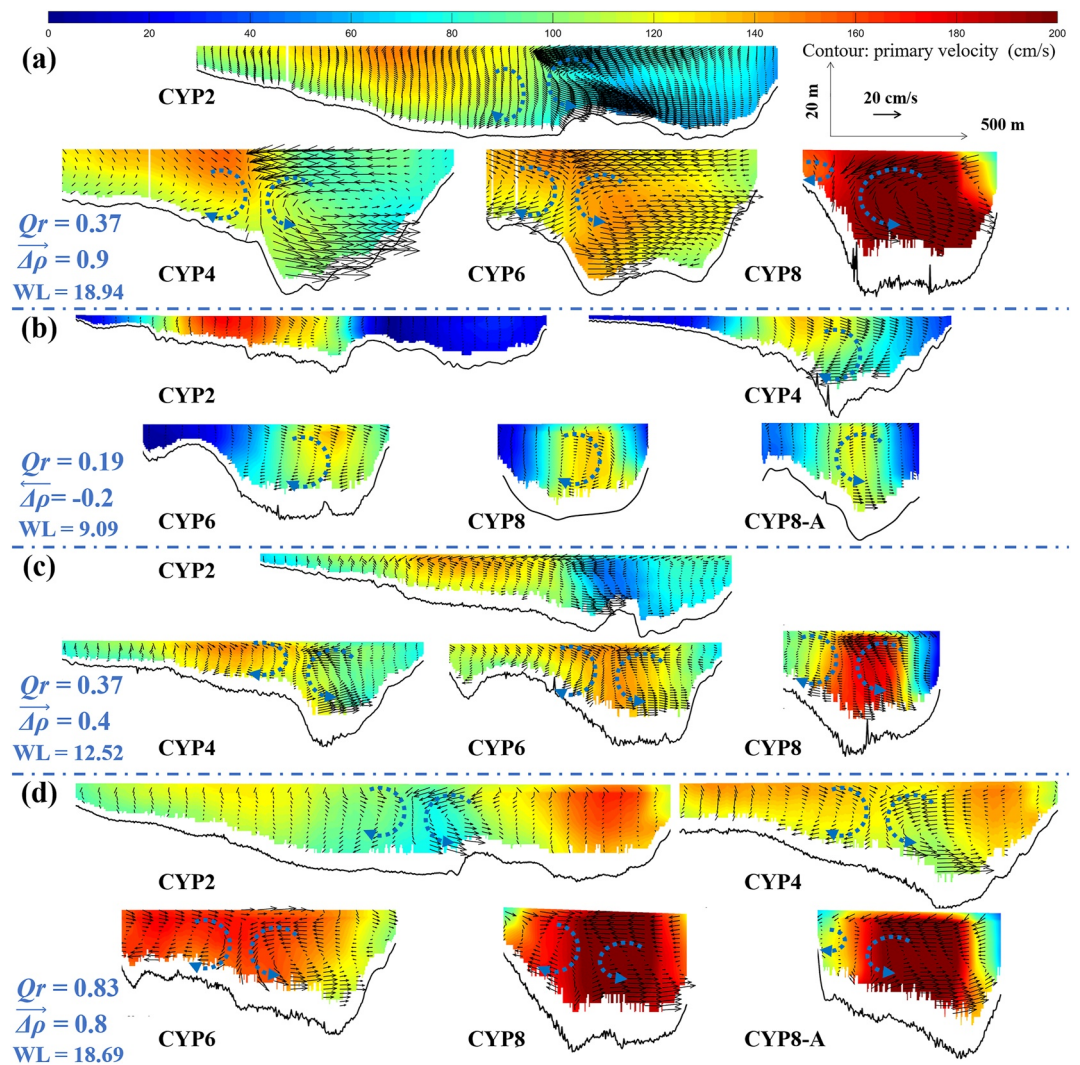


Figure 5. Secondary flows in representative cross sections for (a) Survey 1; (b) Survey 2 2020; (c) Survey 3; (d) Survey 4, looking downstream (Vector: secondary velocity; contour: primary velocity; WL: water level with units of m). The values of $\Delta\rho$ (with an arrow to indicate the direction of decreasing density gradient) and Q_r were consistent with Table 1.

noteworthy that, in Survey 1, the flow originating from the Poyang Lake, with lower water conductivity, seemed to cross over the flow originating from the Yangtze River with higher water conductivity. However, this interesting phenomenon was not obvious in Surveys 3 and 4, where clear mixing interfaces persisted till the end of the marked study area. Comparatively, in Survey 2 under the low flow condition the mixing interface near the water surface disappeared near CYP5 (Figure 3b), suggesting a rapid mixing process. These results were also consistent with the remote sensing images in Figure 4. In Surveys 3 and 4, another clear mixing interface of different conductivity was observed in the tributary (namely Poyang outflow channel) when the large floodplain on the left of the Poyang outflow channel was submerged (Figures 3c and 3d). This interface persisted for a long distance, and the development of this interface could be due to the erosion of sediment on the floodplain. As the water depth increased (Figures 3c to 3d), the conductivity difference in the Poyang outflow decreased from 22 to 9 $\mu\text{S}/\text{cm}$. The mixing interface in the tributary was no longer evident in Survey 1, probably because the large water depth and low flow velocity caused by the backwater effect of Yangtze River on Poyang Lake.

Figure 7 presents the vertical profile of water conductivity at sampling points, in $\mu\text{S}/\text{cm}$. In all the surveys, upstream of CYP2 the distribution of water conductivity in both Yangtze River and Poyang Lake sides was almost uniform at each sampling point without any clear vertical stratification. While on the Yangtze River side in Survey 1, from CYP2 to CYP5, the vertical distribution of conductivity also remained uniform; on the

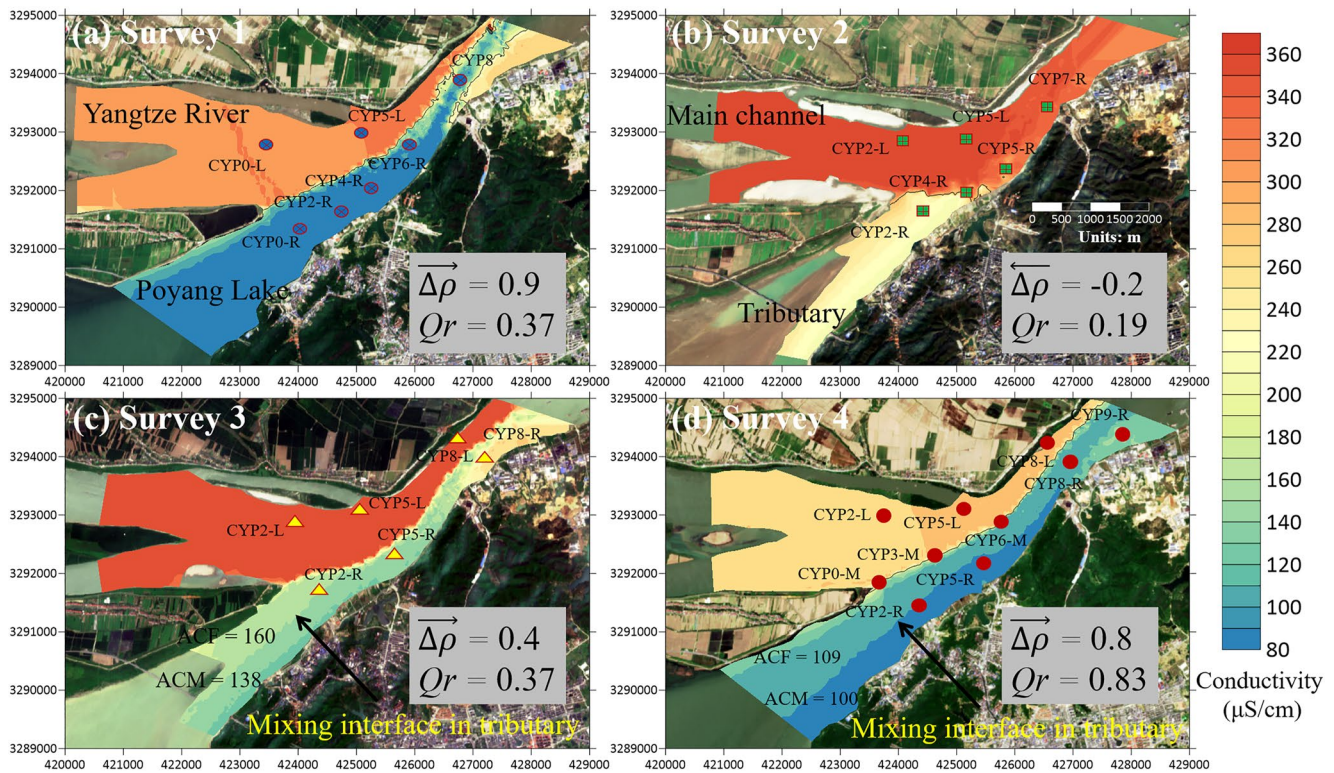


Figure 6. Contours of water conductivity near the water surface during four field surveys. The values of $\Delta\rho$ (with an arrow to indicate the direction of decreasing density gradient) and Q_r were consistent with Table 1. The symbols indicate water chemistry sampling points in each survey. The values of average conductivity in floodplain (ACF) and average conductivity in main channel of Poyang Lake outflow (ACM) were shown with units of $\mu\text{S}/\text{cm}$. Background images were obtained by using remote sensing (Sentinel-1/2 with low cloud cover conditions $<10\%$) during each survey.

Poyang Lake side (i.e., CYP4) the conductivity near the bed was larger than that near the surface. This reveals that entrainment was taking place in the lower part of the water column of Yangtze River with high conductivity. Further downstream such distribution was still observed with a gradual increasing of conductivity over depth that confirms the ongoing development of mixing process (Figure 7a). Such a helical mixing structure was also observed in Figure 6a, clearly speeding up the mixing between the two confluent flows. The counter helix mixing structure seemed to occur in Survey 2 so that at CYP4 in the Poyang Lake side the water conductivity near the water surface in the Poyang Lake side was larger than that near the bed. Rapid mixing was found and the distribution was much more uniform downstream of CYP5 in Survey 2 (Figure 7b) than in the other surveys. The abrupt drop in the conductivity profile in Survey 2 may be caused by small momentum ratio and density difference (as discussed later). In Surveys 3 and 4, vertically uniform profiles were observed for long distance on both sides of the mixing layer. In Survey 3, although the vertical distribution of water conductivity was almost uniform at all sampling points, conductivity values on the Poyang Lake side gradually increased, indicating a slow development of the mixing process between two confluent flows (Figure 7c). In Survey 4 the uniformity conductivity near the bank was seen till the end of the study area in agreement with the contour of conductivity near the water surface (Figure 6d). This revealed a very weak transverse mixing. While the conductivity of the sampling points located near the mixing layer (CYP0/3/6-M) indicated that the mixing layer in Survey 4 also had a significant lateral tilt with a tilt amplitude increasing downstream. This suggests that the mixing process may developed greatly under the surface water. Therefore, the conductivity at the surface water and in a limited number of sampling points may not clearly describe the mixing process in the post-confluence channel and further data analysis is needed.

To gain insights into this difference, the cross-sectional distribution of backscatter (BS) gained by the ADCP measurements was analyzed. BS value could be related to TSS concentration after a proper calibration (Szupiany et al., 2009) and used to identify the location of the mixing interface between two flows of different TSS concentration (Gualtieri et al., 2019). Figure 8 presents the contours of the BS intensity distribution directly measured by RDI at CYP2, CYP4, CYP6, and CYP8 during Surveys 1, 3, and 4. The red and yellow zones indicate the

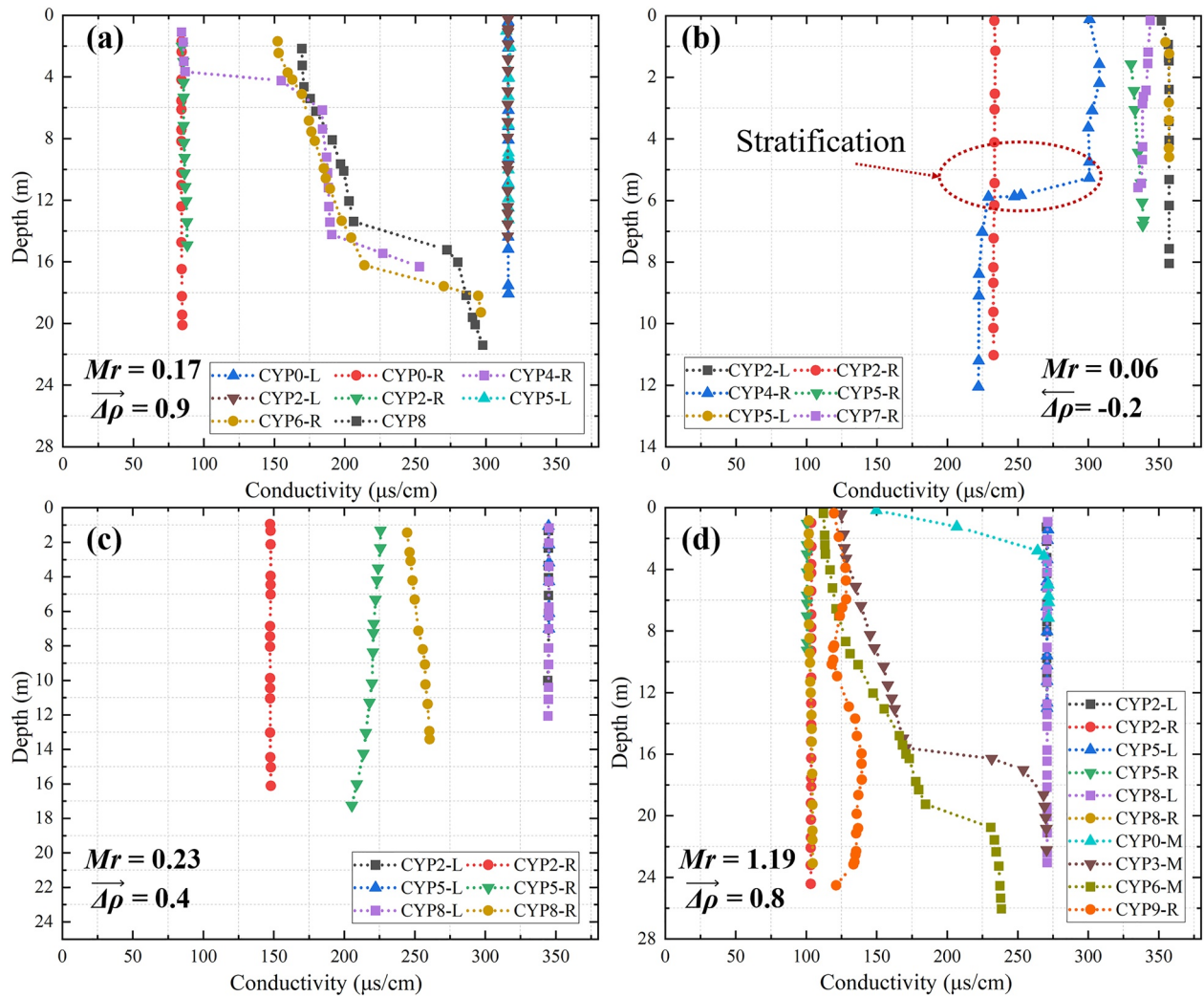


Figure 7. Vertical profiles of conductivity in the field surveys. The locations of the sampling points are marked in Figures 1c and 6. The values of $\Delta\rho$ (with an arrow to indicate the direction of decreasing density gradient) and M_r were consistent with Table 1.

sediment rich waters of the Yangtze River and the blue indicates Poyang Lake waters with low TSS concentration. The dotted lines demarcate the location of the mixing interfaces. The mixing patterns derived from the analysis of the BS data were consistent with the distribution of water conductivity (Figures 6 and 7). In Survey 1 ($\overline{\Delta\rho} = 0.9$), at CYP2 a significant difference in BS between the tributaries was observed across the mixing interface which was tilted obviously. Farther downstream, the mixing interface was subjected to a complex development due to the entrainment of sediment-laden flow at the bed moving from the Yangtze River side into the Poyang Lake pool, which was a kind of “double helix structure” of mixing pattern as aforementioned. At CYP8, the low sediment-laden Poyang Lake waters even moved to the center of river downstream of CYP6, while the sediment-rich Yangtze River waters moved toward the right bank. The same process also occurred in Survey 4 ($\overline{\Delta\rho} = 0.8$). Although the existence of dual-counter rotating cells restricted the mixing process of two flows, the entrainment of sediment-laden flow at the bed moved from the Yangtze River side into the Poyang Lake pool due to the density different. Because the M_r and TSS of the two tributaries in Survey 4 were close (Table 1), the low sediment-laden Poyang Lake waters moved to the center of river till CYP8-A, and the double helix structure was not as obvious as that in Survey 1. In Survey 3 ($\overline{\Delta\rho} = 0.4$), although the mixing layer was also tilted, the sediment-rich waters on the Yangtze River side and the low sediment-laden waters on the Poyang Lake side were constrained on both the sides of the mixing layer by the dual-counter rotating cells, resulting in a slow mixing. The reason for the difference results between Survey 1, 4 will be discussed later.

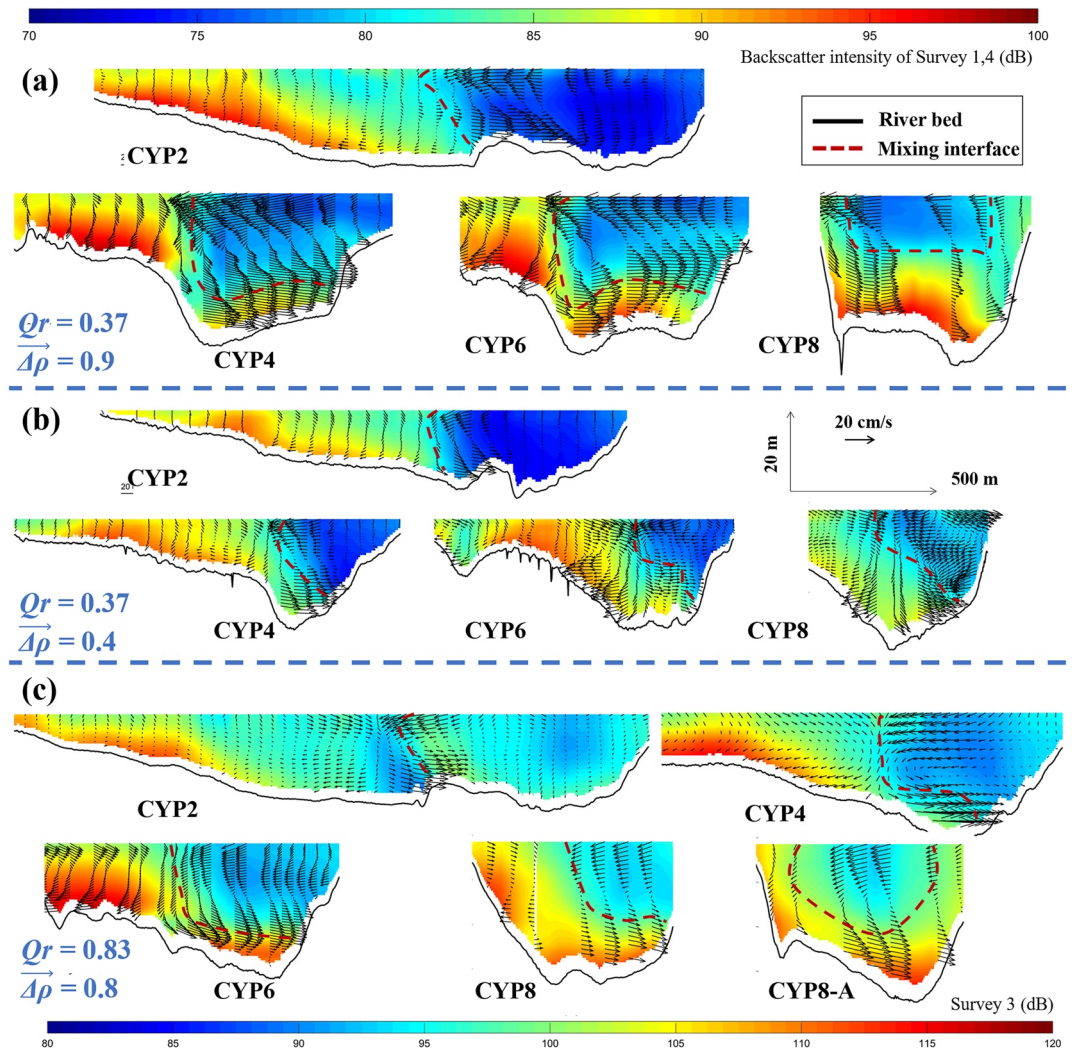


Figure 8. Distribution of the backscatter intensity and secondary flow for transects CYP2, CYP4, CYP6, and CYP8 during Survey 1 (a), Survey 3 (b), and Survey 4 (c; CYP8-A) Looking downstream (Vector: secondary velocity; contour: backscatter intensity). Note the use of different scales for different surveys (Top color bar for Survey 1, and 4; Bottom color bar for Survey 3). The values of $\Delta\rho$ (with an arrow to indicate the direction of decreasing density gradient) and Q_r were consistent with Table 1.

3.5. Characterization of Global Surface Mixing Rate

Mixing at confluences is commonly characterized based on the streamwise variation of the standard deviation of a tracer (Gaudet & Roy, 1995; Horna-Munoz et al., 2020; Lewis et al., 2020; Lewis & Rhoads, 2015). In the present study, the streamwise development of mixing is estimated using a normalized mixing metric developed by Lewis and Rhoads (2015) and Lewis et al. (2020). The metric is based upon the calculation of the standard deviation of the conductivity at each cross-section (σ_x) in the CHZ as well as at an upstream composite cross-section consisting of conductivity for the two incoming flows (σ_{us}). The standard deviation for the composited cross section was calculated using more than 500 values of the conductivity which were measured by the EXO2 probe during the investigation of bathymetry and distribution of water chemistry parameters near the water surface. The proportion of the 500 values assigned to each tributary flow depends upon the ratio of cross-sectional areas of these flows. The surface mixing rate between the confluence apex and a downstream cross-section is computed as a percentage (m) based on the change in the normalized standard deviation from the upstream section to the current section: $m = (\sigma_{us} - \sigma_x) / (\sigma_{us}) \times 100$. If the cross section of interest has the same tracer standard deviation (σ_x) as the hypothetical upstream cross section (σ_{us}), no mixing occurs, and m equals 0. If the nondimensional conductivity field at a cross section is completely uniform ($\sigma_x \approx 0$), mixing is complete and m equals 100.

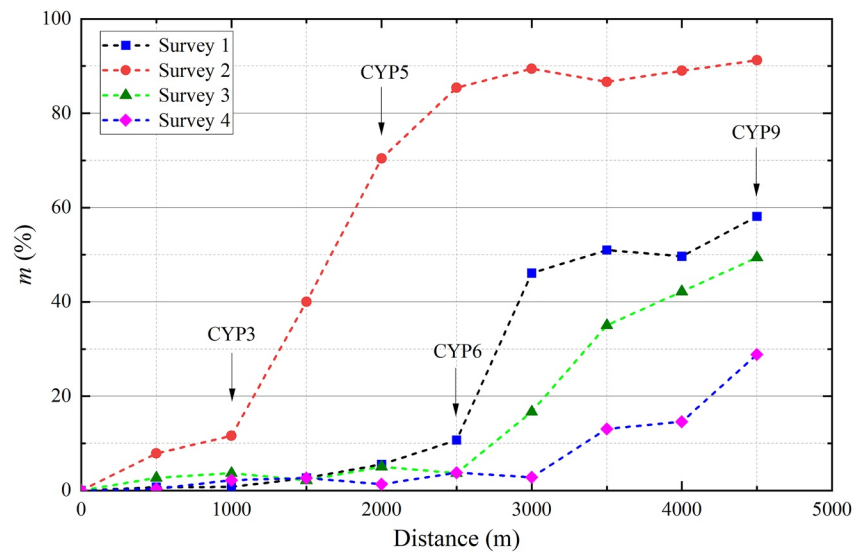


Figure 9. Longitudinal distribution of the surface mixing rate given as a percentage of mixed conductivity at the surface of cross section, m . The distance is measured along the centerline of the mixing interface near the water surface with distance = 0 at the confluence apex (CYP1).

Figure 9 presents the longitudinal distribution of m for the four surveys, and the spatial change of m with distance can reflect the mixing rate near the water surface (Rhoads & Johnson, 2018). The plot confirms that among the four surveys, Survey 2 had the most rapid mixing as it was almost completed (m approximately 70%) at CYP5. For the other three surveys, upstream of CYP6, the mixing rate was about the same. However, farther downstream it increases significantly in Survey 1, which was related to the double helix structure of mixing pattern. At the downstream end of the study area that percentage was of approximately 90% in Survey 2, while for Survey 1, Survey 3 and Survey 4 it was in the order of 60%, 50% and 30%, respectively.

4. Discussion on the Cause of Mixing Patterns

Momentum flux ratio, channel-scale secondary cells, and density difference are common factors that affect the mixing processes between two confluent flows (Cheng & Constantinescu, 2021; Constantinescu et al., 2012, 2014, 2016; Horna-Munoz et al., 2020; Lane et al., 2008; Lewis et al., 2020; Lewis & Rhoads, 2015; Rhoads & Sukhodolov, 2008). In this section, attempts have made to determine the possible causes that result in the different mixing patterns of these four surveys.

4.1. Momentum Flux Ratio

Laboratory (Best, 1987, 1988), field (Gualtieri et al., 2018; Lane et al., 2008; Lewis & Rhoads, 2015; Rhoads, 1996; Rhoads & Kenworthy, 1998; Rhoads & Sukhodolov, 2001; Yuan et al., 2021), and numerical (Bradbrook et al., 2000, 2001; Constantinescu et al., 2016) studies of river confluences have shown that the M_r has a critical effect on the interaction between two confluent streams. The shear layer presents high levels of turbulence and large-scale coherent structures, which enhanced lateral mixing. For all the surveys, a distinct velocity contrast exists between the two confluent flows. The depth-averaged velocity patterns show that the shear layer is relatively aligned with the upstream mixing interface, especially in Survey 2. The location of the shear layer and mixing interface shifted toward the right bank for low M_r (Surveys 1, 2, 3) and toward the center of the post-confluence channel for high M_r (Survey 4). Therefore, we can infer that M_r dominates the transversal location of the mixing interface. Furthermore, in Surveys 1, 3, 4 complete re-alignment of the Poyang Lake flow with the Yangtze River post-confluence channel occurred near CYP7 and the shear layers disappears, even though the mixing interface extended downstream till the end of the study reach. That is, lateral transport associated with these coherent structures within the shear layer is insufficient to produce conspicuous mixing between

two flows, suggested by Lane et al. (2008). Therefore, other driving factors which cause different mixing patterns and rates in the four surveys need further discussion.

4.2. Channel-Scale Secondary Cells

The results for all four surveys indicated that the development of secondary flow can play an important role in mixing dynamics. The presence of single channel-scale secondary cell (Survey 2), or dual secondary cells (Surveys 1, 3, and 4) contribute to the corresponding mixing patterns between the two confluent flows. The helical motions on the left side restricted the size of the core of high sediment concentration. The downwelling flows between the dual counter-rotating helical cells acted as a barrier preventing mixing between the two rivers (Yuan et al., 2021). These results are in agreement with recent studies on mixing at other confluences, which have indicated that little to no mixing takes place within the CHZ when dual helical cells develop (Chen et al., 2017; Konsoer & Rhoads, 2014; Rhoads & Johnson, 2018; Riley et al., 2015). However, as the helical cell from the Poyang Lake became dominant and almost occupied the whole cross section (after CYP6 in Survey 1 and after CYP8 in Survey 4), mixing was enhanced. The flow from the Yangtze River was advected near the bed into the flow from the lateral tributary, thereby contributing to the “double helix” structure observed in Surveys 1 and 4 (Figures 8a and 8c). On the other hand, there were always dual counter-rotating cells, extending till the end of study area in Survey 3, which resulting in a relatively slow mixing rate (Figures 6 and 8). That is, dual counter-rotating helical cells limit the mixing processes at the post-confluence channel (Surveys 1, 3 and 4), especially when $\Delta\rho$ is small (Survey 3). At confluences, subsurface thermal mixing is greatly enhanced by secondary currents associated with helical motion, especially when a single dominant cell develops (Lewis & Rhoads, 2015; Rhoads & Johnson, 2018). Although the main cause of rapid mixing process in Survey 2 were the small momentum ratio ($M_r = 0.06$) and density effect, the development of a curvature-driven large-scale helical motion also played an important role. This aspect has been supported by recent field studies on mixing at confluences (Herrero et al., 2018; Lane et al., 2008; Sukhodolov & Sukhodolova, 2019).

4.3. Density Difference

Past literature suggested that the hydrodynamics and mixing processes at confluences are affected by density difference (Gualtieri et al., 2019; Jiang et al., 2022; Lewis & Rhoads, 2015; Lyubimova et al., 2014; Ramón et al., 2013, 2014). The lock-exchange mechanism generated by the density difference, may work with/against the curvature-induced structure of helical cells in the Yangtze River (Horna-Munoz et al., 2020). The Yangtze River flow had large density effect in Surveys 1 and 4 ($Fr_d \sim 2.2/2.9$), and the advective mixing by helical motion was impeded as the lock-exchange acted against this pattern (Figure 10a). Density differences promoted outward movement of fluid near the bed and inward movement of fluid near the surface from the Poyang Lake having a lower density, in opposition to the influence of helical motion on near-surface and near-bed flow. As the helical motion decayed downstream, the warm, less dense water of Poyang Lake gradually moved to the middle of the channel near the surface while cool, dense water of Yangtze River crossed the bed and moved to the right bank, and a single channel-scale secondary flow formed downstream (after CYP6 in Survey 1; after CYP8 in Survey 4) to enhance the water mixing (Figures 8a and 8c). Although the backscatter profiles (Figure 8) also suggest that the core of lighter fluid was confined in the center of the channel in Figure 10a, this may be only until the denser flow upwells. Eventually, the lighter fluid will spread out laterally to form a thin layer near the surface if there is no force to keep it there against the pull of gravity. It is worth noting that the surface mixing rate of Survey 4 was the slowest, which may be related to the largest momentum flux ratio ($M_r \sim 1$) increasing the mixing distance. Therefore, it is improper to indicate the mixing rate using remote sensing images or surface water quality data at large-scale river confluences, especially those with density differences. Even though Fr_d value in the Survey 3 ($Fr_d \sim 2.9$) was close to that in Surveys 1 and 4, it also mixed slowly without a clear stratification (Figures 7c and 8b). On the one hand, the density effects might have been weakened by the larger relative bed roughness associated with the lower water depth in Survey 3 (Best & Roy, 1991; Constantinescu et al., 2016). On the other hand, the density effect of Survey 3 may not be as large as the density Froude number indicated (Duguay et al., 2022b; Pouchoulin et al., 2020).

In Survey 2 ($M_r = 0.06$), the rapid mixing can be related to the large lateral expansion of the Yangtze River into the Poyang Lake portion of the confluence due to the large momentum and density difference, resulting in a vertical stratification at CYP4 (Figure 7b). The abrupt drop in the conductivity profile in Survey 2 might not be

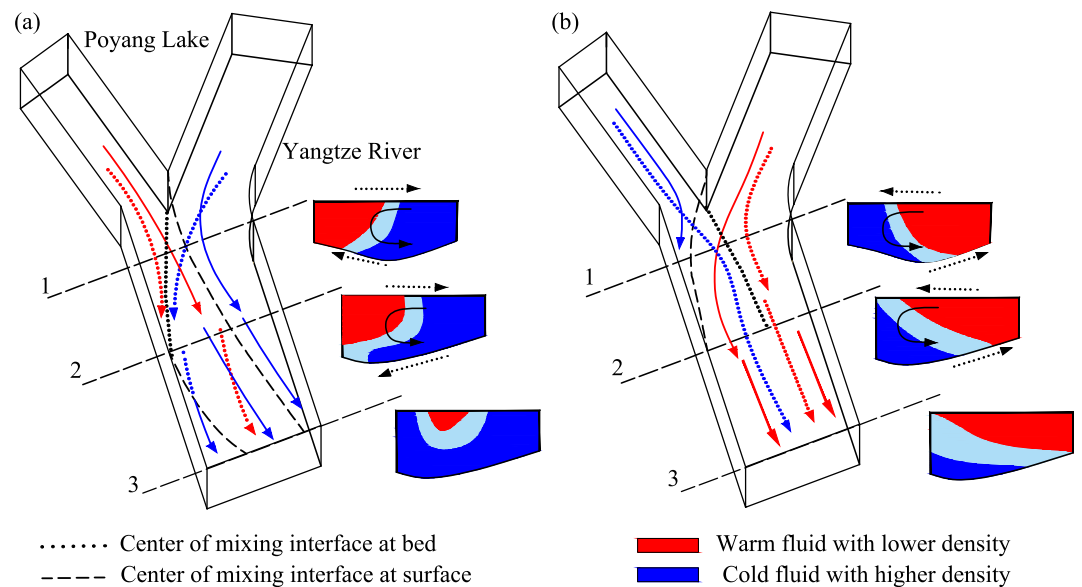


Figure 10. Conceptual model showing patterns of lateral mixing between two flows with different densities at the confluence of Yangtze River and Poyang Lake. (a) Yangtze River contains fluid denser than the Poyang Lake, and (b) Poyang Lake contains fluid denser than the Yangtze River. Red arrows correspond to flow from the Yangtze River and blue arrows correspond to flow in the Poyang Lake, with solid arrows representing flow near the surface and dashed arrows representing flow near the bed. Curved arrows in cross-section denote strong, curvature-induced cells of helical flow, while the dashed arrows show the development of the near-bed and free-surface intrusions associated with the lock-exchange like flow. Dark blue corresponds to unmixed fluid with cold temperature and higher density, Red corresponds to unmixed fluid with warm temperature and lower density, and light blue corresponds to mixed fluid between the two unmixed fluid mentioned above.

only caused by momentum ratio effects that could cause a much less abrupt gradient due to turbulent momentum exchange along the mixing interface. The rapid drop is more consistent with the interface between stratified layers of a lighter and a denser fluid due to the density difference. Despite the density effect ($Fr_d \sim 6.2 > 5$) was weaker than that in higher flow conditions, density difference and curvature-induced cells of helical flow were working together (Figure 10b). Both the lock exchange and the helical cell moved from Poyang Lake to Yangtze River at the bed and from Yangtze River to Poyang Lake at the free surface. In addition, the M_r was the lowest and Yangtze River pushed strongly against Poyang Lake side to form a two-layer structure. Hence, the penetration of the Yangtze River flow at the free surface was enhanced (Lane et al., 2008). This explains the fastest mixing found in Survey 2.

From the above results and discussion, it is possible to assess the contribution of the momentum flux ratio, large-scale secondary cells, and the density effects to river mixing patterns at the large-scale river confluence of Yangtze River and Poyang Lake. Table 2 lists the causes of different mixing patterns in these four surveys. A summary of the main causes of mixing patterns when mixing is slow or rapid is given in Table 2.

5. Conclusion

Four field surveys were conducted to investigate the lateral mixing dynamics of a large river confluence (combined width ~ 2.5 km) between the Yangtze River (the largest river in China) and the outflow channel of Poyang Lake (the largest freshwater lake in China). Those surveys were carried out during medium and high (Survey 1, 3, and 4), as well as low flow condition (Survey 2).

The main important conclusions drawn from this study are:

1. Signatures of the water chemistry of the Yangtze River and Poyang Lake were mixing slowly (with mixing distance >5 km, limited by the range of study area) during medium and high flow conditions and presents a double helix distribution in Surveys 1 and 4, but were mixing rapidly and stratified vertically near the mixing interface during low flow conditions (with mixing distance ~ 2.5 km).

Table 2
Causes of Different Mixing Patterns in These Four Surveys

Survey name	Surface mixing rate	Causes of mixing pattern		
		Momentum ratio	Secondary flows	Density effects
Survey 1	Fast	Medium	Dual cells turning to single cell; beneficial to the fast mixing downstream	Large; beneficial to the transfer from dual cells to single cell and the water mixing
Survey 2	Fastest	Very small; dominating the fast mixing	Single cell; beneficial to the fast mixing	Small; beneficial to the single cell and the water mixing
Survey 3	Slow	Medium	Dual cells; beneficial to the slow mixing	Large; beneficial to the water mixing
Survey 4	Slowest	Approximately 1; dominating the slow mixing	Dual cells; beneficial to the slow mixing	Large; beneficial to the water mixing

- All the mixing processes around the confluence are controlled by a complex interaction among the momentum flux ratio, secondary flow and the lock-exchange process due to the density contrast between the tributaries.
- The momentum flux ratio affects the position of the mixing layer and influences the mixing process in the post-confluence channel. Larger momentum difference can produce larger penetration of the Yangtze River under the Poyang Lake outlet, resulting in larger velocity difference and rapid mixing rate.
- The dual counter-rotating helical cells in higher flow conditions prevent mixing process due to the downwelling flows between them acting as a barrier. As an anticlockwise channel-scale sized helical cell becomes dominant, mixing is enhanced; flow from the Yangtze River is advected near the bed into flow from the lateral tributary.
- The lock exchange generated by density difference affects the mixing patterns. It can work together/against the secondary flow induced by flow curvature. When flow from the Yangtze River has a lower density than flow in the Poyang Lake, buoyant forces reinforce secondary currents, or else, they act against these secondary currents.

Data Availability Statement

The data are available for download: <https://doi.org/10.5281/zenodo.6866986>.

Acknowledgments

This research was funded by the National Key R&D Program of China (Grant 2022YFC3200032), National Natural Science Foundation of China (51779080; U2040205; 52079044), the Fundamental Research Funds for the Central Universities (20195025712), the 111 Project (B17015), the Fok Ying Tung Education Foundation (520013312), and the Jiangsu Province Project (2021001). The authors would like to thank Professor Bidya Sagar Pani of the Indian Institute of Technology-Bombay for help in revising this work. Thanks are also extended to Yunqiang Zhu, Yuchen Zheng, Yihong Chen, Chenhui Wang, Hao Wang, Chun Li, and Jiaming Yang of Hohai University for their support during the field surveys.

References

- Ashmore, P. E., Ferguson, R. I., Prestegard, K. L., Ashworth, P. J., & Paola, C. (1992). Secondary flow in anabranch confluences of a braided, gravel-bed stream. *Earth Surface Processes and Landforms*, 17, 299–311. <https://doi.org/10.1002/esp.3290170308>
- Best, J. L. (1987). Flow dynamics at river channel confluences: Implications for sediment transport and bed morphology. In F. G. Etheridge, R. M. Flores, & M. D. Harvey (Eds.) *Recent Developments in Fluvial Sedimentology*. (Vol. 39, pp. 27–35). SEPM (Society of Economic Paleontologists and Mineralogists). <https://doi.org/10.2110/pec.87.39.0027>
- Best, J. L. (1988). Sediment transport and bed morphology at river channel confluences. *Sedimentology*, 35(3), 481–498. <https://doi.org/10.1111/j.1365-3091.1988.tb00999.x>
- Best, J. L., & Roy, A. G. (1991). Mixing-layer distortion at the confluence of channels of different depth. *Nature*, 350(6317), 411–413. <https://doi.org/10.1038/350411a0>
- Bing, J. P. (2018). *The evolution trend and regulation effect of the Yangtze River-Poyang Lake relationship*. Wuhan University.
- Biron, P., Best, J. L., & Roy, A. G. (1996). Effects of bed discordance on flow dynamics at open channel confluences. *Journal of Hydraulic Engineering*, 122(12), 676–682. [https://doi.org/10.1061/\(asce\)0733-9429\(1996\)122:12\(676\)](https://doi.org/10.1061/(asce)0733-9429(1996)122:12(676))
- Biron, P., Roy, A. G., & Best, J. L. (1996). Turbulent flow structure at concordant and discordant open-channel confluences. *Experiments in Fluids*, 21(6), 437–446. <https://doi.org/10.1007/bf00189046>
- Biron, P. M., Buffin-Bélanger, T., & Martel, N. (2019). Three-dimensional turbulent structures at a medium-sized confluence with and without an ice cover. *Earth Surface Processes and Landforms*, 44(15), 3042–3056. <https://doi.org/10.1002/esp.4718>
- Bouchez, J., Lajeunesse, E., Gaillardet, J., France-Lanord, C., Dutra-Maia, P., & Maurice, L. (2010). Turbulent mixing in the Amazon River: The isotopic memory of confluences. *Earth and Planetary Science Letters*, 290(1–2), 37–43. <https://doi.org/10.1016/j.epsl.2009.11.054>
- Bradbrook, K. F., Lane, S. N., & Richards, K. S. (2000). Numerical simulation of three-dimensional, time-averaged flow structure at river channel confluences. *Water Resources Research*, 36(9), 2731–2746. <https://doi.org/10.1029/2000wr900011>
- Bradbrook, K. F., Lane, S. N., Richards, K. S., Biron, P. M., & Roy, A. G. (2001). Role of bed discordance at asymmetrical river confluences. *Journal of Hydraulic Engineering*, 127(5), 351–368. [https://doi.org/10.1061/\(asce\)0733-9429\(2001\)127:5\(351\)](https://doi.org/10.1061/(asce)0733-9429(2001)127:5(351))
- Chen, X., Zhu, D. Z., & Steffler, P. M. (2017). Secondary currents induced mixing at channel confluences. *Canadian Journal of Civil Engineering*, 44, 1071–1083. <https://doi.org/10.1139/cjce-2016-0228>

- Cheng, Z., & Constantinescu, G. (2018). Stratification effects on flow hydrodynamics and mixing at a confluence with a highly discordant bed and a relatively low velocity ratio. *Water Resources Research*, *54*, 4537–4562. <https://doi.org/10.1029/2017WR022292>
- Cheng, Z., & Constantinescu, G. (2020). Stratification effects on hydrodynamics and mixing at a river confluence with discordant bed. *Environmental Fluid Mechanics*, *20*(4), 843–872. <https://doi.org/10.1007/s10652-019-09725-6>
- Cheng, Z., & Constantinescu, G. (2021). Shallow mixing layers between non-parallel streams in a flat-bed wide channel. *Journal of Fluid Mechanics*, 916. <https://doi.org/10.1017/jfm.2021.254>
- Constantinescu, G., Miyawaki, S., Rhoads, B., & Sukhodolov, A. (2012). Numerical analysis of the effect of momentum ratio on the dynamics and sediment-entrainment capacity of coherent flow structures at a stream confluence. *Journal of Geophysical Research*, *117*, F04028. <https://doi.org/10.1029/2012JF002452>
- Constantinescu, G., Miyawaki, S., Rhoads, B., & Sukhodolov, A. (2014). Numerical evaluation of the effects of planform geometry and inflow conditions on flow, turbulence structure, and bed shear velocity at a stream confluence with a concordant bed. *Journal of Geophysical Research: Earth Surface*, *119*, 2079–2097. <https://doi.org/10.1002/2014JF003244>
- Constantinescu, G., Miyawaki, S., Rhoads, B., & Sukhodolov, A. (2016). Influence of planform geometry and momentum ratio on thermal mixing at a stream confluence with a concordant bed. *Environmental Fluid Mechanics*, *16*(4), 845–873. <https://doi.org/10.1007/s10652-016-9457-0>
- Constantinescu, G., Miyawaki, S., Rhoads, B., Sukhodolov, A., & Kirkil, G. (2011). Structure of turbulent flow at a river confluence with momentum and velocity ratios close to 1: Insight provided by an eddy resolving numerical simulation. *Water Resources Research*, *5*, W05507. <https://doi.org/10.1029/2010WR010018>
- De Serres, B., Roy, A. G., Biron, P. M., & Best, J. L. (1999). Three-dimensional structure of flow at a confluence of river channels with discordant beds. *Geomorphology*, *26*(4), 313–335. [https://doi.org/10.1016/s0169-555x\(98\)00064-6](https://doi.org/10.1016/s0169-555x(98)00064-6)
- Duguay, J., Biron, P. M., & Lacey, J. (2022a). Aerial observations and numerical simulations confirm density-driven streamwise vortices at a river confluence. *Water Resources Research*, *58*(7), e2021WR031527. <https://doi.org/10.1029/2021wr031527>
- Duguay, J., Biron, P. M., & Lacey, J. (2022b). Impact of density gradients on the secondary flow structure of a river confluence. *Water Resources Research*, *58*, e2022WR032720. <https://doi.org/10.1029/2022WR032720>
- Fang, C. M., Cao, W. H., Mao, J. X., & Li, H. J. (2012). Relationship between Poyang Lake and influence of three Georges reservoir. *Shuili Xuebao (Journal of Hydraulic Engineering)*, *43*(2), 175–181.
- Ford, D. E., & Johnson, M. C. (1983). *An assessment of reservoir density currents and inflow processes*. Ford Thornton Norton and Associates Ltd.
- Gaspar, E. (1987). *Modern trends in tracer hydrology*. CRC Press.
- Gaudet, J. M., & Roy, A. G. (1995). Effect of bed morphology on flow mixing length at river confluences. *Nature*, *373*(6510), 138–139. <https://doi.org/10.1038/373138a0>
- Gualtieri, C., Filizola, N., de Oliveira, M., Santos, A. M., & Ianniruberto, M. (2018). A field study of the confluence between Negro and Solimões Rivers. Part 1: Hydrodynamics and sediment transport. *Comptes Rendus Geoscience*, *350*(1–2), 31–42. <https://doi.org/10.1016/j.crte.2017.09.015>
- Gualtieri, C., Ianniruberto, M., & Filizola, N. (2019). On the mixing of rivers with a difference in density: The case of the Negro/Solimões confluence, Brazil. *Journal of Hydrology*, *578*, 124029. <https://doi.org/10.1016/j.jhydrol.2019.124029>
- Gualtieri, C., Ianniruberto, M., Filizola, N., Santos, R., & Endreny, T. (2017). Hydraulic complexity at a large river confluence in the Amazon basin. *Ecology*, *10*(7), e1863. <https://doi.org/10.1002/eco.1863>
- Guillén-Ludeña, S., Cheng, Z., Constantinescu, G., & Franca, M. J. (2017). Hydrodynamics of mountain-river confluences and its relationship to sediment transport. *Journal of Geophysical Research: Earth Surface*, *122*, 901–924. <https://doi.org/10.1002/2016JF004122>
- Guillén-Ludeña, S., Franca, M. J., Cardoso, A. H., & Schleiss, A. J. (2016). Evolution of the hydromorphodynamics of mountain river confluences for varying discharge ratios and junction angles. *Geomorphology*, *255*, 1–15. <https://doi.org/10.1016/j.geomorph.2015.12.006>
- Guo, H., Hu, Q., Zhang, Q., & Feng, S. (2012). Effects of the three gorges dam on Yangtze River flow and River interaction with Poyang Lake, China: 2003–2008. *Journal of Hydrology*, *416*, 19–27. <https://doi.org/10.1016/j.jhydrol.2011.11.027>
- Herrero, H. S., García, C. M., Pedocchi, F., Lopez, G., Szupiany, R. N., & Pozzi-Piacenza, C. E. (2016). Flow structure at a confluence: Experimental data and the bluff body analogy. *Journal of Hydraulic Research*, *54*, 263–274. <https://doi.org/10.1080/00221686.2016.1146804>
- Herrero, H. S., Lozada, J. M. D., García, C. M., Szupiany, R. N., Best, J., & Pagot, M. (2018). The influence of tributary flow density differences on the hydrodynamic behavior of a confluent meander bend and implications for flow mixing. *Geomorphology*, *304*, 99–112. <https://doi.org/10.1016/j.geomorph.2017.12.025>
- Horna-Munoz, D., Constantinescu, G., Rhoads, B., Lewis, Q., & Sukhodolov, A. (2020). Density effects at a concordant bed natural river confluence. *Water Resources Research*, *56*(4), e2019WR026217. <https://doi.org/10.1029/2019wr026217>
- Ianniruberto, M., Trevethan, M., Pinheiro, A., Andrade, J. F., Dantas, E., Filizola, N., et al. (2018). A field study of the confluence between Negro and Solimões Rivers. Part 2: Bed morphology and stratigraphy. *Comptes Rendus Geoscience*, *350*(1–2), 43–54. <https://doi.org/10.1016/j.crte.2017.10.005>
- Jamieson, E. C., Rennie, C. D., Jacobson, R. B., & Townsend, R. D. (2011). 3-D flow and scour near a submerged wing dike: ADCP measurements on the Missouri river. *Water Resources Research*, *47*(7). <https://doi.org/10.1029/2010wr010043>
- Jiang, C., Constantinescu, G., Yuan, S., & Tang, H. (2022). Flow hydrodynamics, density contrast effects and mixing at the confluence between the Yangtze River and the Poyang Lake channel. *Environmental Fluid Mechanics*, 1–29.
- Kell, G. S. (1975). Density, thermal expansivity, and compressibility of liquid water from 0. deg. to 150. deg. correlations and tables for atmospheric pressure and saturation reviewed and expressed on 1968 temperature scale. *Journal of Chemical and Engineering Data*, *20*(1), 97–105. <https://doi.org/10.1021/je60064a005>
- Kenworthy, S. T., & Rhoads, B. L. (1995). Hydrologic control of spatial patterns of suspended sediment concentration at a small stream confluence. *Journal of Hydrology*, *168*, 251–263. [https://doi.org/10.1016/0022-1694\(94\)02644-q](https://doi.org/10.1016/0022-1694(94)02644-q)
- Konsoer, K. M., & Rhoads, B. L. (2014). Spatial-temporal structure of mixing interface turbulence at two large river confluences. *Environmental Fluid Mechanics*, *14*(5), 1043–1070. <https://doi.org/10.1007/s10652-013-9304-5>
- Lane, S. N., Bradbrook, K. F., Richards, K. F., Biron, P. M., & Roy, A. G. (2000). Secondary circulation cells in river channel confluence: Measurement artifacts or coherent flow structures? *Hydrological Processes*, *14*, 2047–2071. [https://doi.org/10.1002/1099-1085\(20000815/30\)14:11/12<2047::aid-hyp54>3.0.co;2-4](https://doi.org/10.1002/1099-1085(20000815/30)14:11/12<2047::aid-hyp54>3.0.co;2-4)
- Lane, S. N., Parsons, D. R., Best, J. L., Orfeo, O., Kostaschuk, R. A., & Hardy, R. J. (2008). Causes of rapid mixing at a junction of two large rivers: Río Paraná and Río Paraguay, Argentina. *Journal of Geophysical Research*, *113*, F02019. <https://doi.org/10.1029/2006jf000745>
- Laraque, A., Guyot, J. L., & Filizola, N. (2009). Mixing processes in the Amazon River at the confluences of the Negro and Solimões Rivers, Encontro das Águas, Manaus, Brazil. *Hydrological Processes: International Journal*, *23*(22), 3131–3140. <https://doi.org/10.1002/hyp.7388>
- Leite Ribeiro, M., Blanckaert, K., Roy, A. G., & Schleiss, A. J. (2012). Flow and sediment dynamics in channel confluences. *Journal of Geophysical Research: Earth Surface*, *117*(F1). <https://doi.org/10.1029/2011JF002171>

- Lewis, Q., Rhoads, B., Sukhodolov, A., & Constantinescu, G. (2020). Advective lateral transport of streamwise momentum governs mixing at small river confluences. *Water Resources Research*, 56(9), e2019WR026817. <https://doi.org/10.1029/2019wr026817>
- Lewis, Q. W., & Rhoads, B. L. (2015). Rates and patterns of thermal mixing at a small stream confluence under variable incoming flow conditions. *Hydrological Processes*, 29(20), 4442–4456. <https://doi.org/10.1002/hyp.10496>
- Li, K., Tang, H., Yuan, S., Xiao, Y., Xu, L., Huang, S., et al. (2022). A field study of near-junction-apex flow at a large river confluence and its response to the effects of floodplain flow. *Journal of Hydrology*, 610, 127983. <https://doi.org/10.1016/j.jhydrol.2022.127983>
- Lyubimova, T., Lepikhin, A., Kononov, V., Parshakova, Y., & Tiunov, A. (2014). Formation of the density currents in the zone of confluence of two rivers. *Journal of Hydrology*, 508, 328–342. <https://doi.org/10.1016/j.jhydrol.2013.10.041>
- McLelland, S. J., Ashworth, P., & Best, J. L. (1996). The origin and downstream development of coherent flow structures at channel junctions. In P. Ashworth, S. J. Bennett, J. L. Best, & S. J. McLelland (Eds.), *Coherent flow structures in open channels* (pp. 459–490). John Wiley and Sons.
- McLelland, S. J., Ashworth, P. J., Best, J. L., Roden, J., & Klaassen, G. J. (1999). Flow structure and transport of sand-grade suspended sediment around an evolving braid bar, Jamuna River, Bangladesh. *Fluvial sedimentology*, 6, 43–57.
- Moody, J. A. (1995). Observations of mixing processes downstream from the confluence of the Mississippi and St. Croix rivers. *Geophysical Monograph Series*, 94, 275–286.
- Moreira, S., Schultze, M., Rahn, K., & Boehrer, B. (2016). A practical approach to lake water density from electrical conductivity and temperature. *Hydrology and Earth System Sciences*, 20(7), 2975–2986. <https://doi.org/10.5194/hess-20-2975-2016>
- Mosley, M. P. (1976). An experimental study of channel confluences. *The Journal of Geology*, 84(5), 535–562. <https://doi.org/10.1086/628230>
- Paola, C. (1997). When streams collide. *Nature*, 387, 232–233. <https://doi.org/10.1038/387232a0>
- Parsons, D. R., Best, J. L., Lane, S. N., Orfeo, O., Hardy, R. J., & Kostaschuk, R. (2007). Form roughness and the absence of secondary flow in a large confluence–difffluence, Rio Paraná, Argentina. *Earth Surface Processes and Landforms*, 32(1), 155–162. <https://doi.org/10.1002/esp.1457>
- Parsons, D. R., Jackson, P. R., Czuba, J. A., Engel, F. L., Rhoads, B. L., Oberg, K. A., et al. (2013). Velocity mapping toolbox (VMT): A processing and visualization suite for moving-vessel ADCP measurements. *Earth Surface Processes and Landforms*, 38, 1244–1260. <https://doi.org/10.1002/esp.3367>
- Pouchoulin, S., LeCoz, J., Mignot, E., Gond, L., & Riviere, N. (2020). Predicting transverse mixing efficiency downstream of a river confluence. *Water Resources Research*, 56(10), e2019WR026367. <https://doi.org/10.1029/2019WR026367>
- Prats, J., Armengol, J., Marce, R., Sánchez-Juny, M., & Dolz, J. (2010). Dams and reservoirs in the lower Ebro River and its effects on the river thermal cycle. *Hdb. Environmental Chemistry*, 13, 77–95. https://doi.org/10.1007/698_2010_68
- Ramón, C. L., Armengol, J., Dolz, J., Prats, J., & Rueda, F. (2014). Mixing dynamics at the confluence of two large rivers undergoing weak density variations. *Journal of Geophysical Research: Oceans*, 119, 2386–2402. <https://doi.org/10.1002/2013JC009488>
- Ramón, C. L., Hoyer, A. B., Armengol, J., Dolz, J., & Rueda, F. J. (2013). Mixing and circulation at the confluence of two rivers entering a meandering reservoir. *Water Resources Research*, 49, 1429–1445. <https://doi.org/10.1002/wrcr.20131>
- Ramón, C. L., Prats, J., & Rueda, F. (2016). The influence of flow inertia, buoyancy, wind, and flow unsteadiness on mixing at the asymmetrical confluence of two large rivers. *Journal of Hydrology*, 539, 11–26.
- Rathbun, R. E., & Rostad, C. E. (2004). Lateral mixing in the Mississippi river below the confluence with the Ohio river. *Water Resources Research*, 40, W05207. <https://doi.org/10.1029/2003WR002381>
- Rennie, C. D., & Church, M. (2010). Mapping spatial distributions and uncertainty of water and sediment flux in a large gravel bed river reach using an acoustic Doppler current profiler. *Journal of Geophysical Research: Earth Surface*, 115(F3). <https://doi.org/10.1029/2009jf001556>
- Rhoads, B. L. (1996). Mean structure of transport-effective flows at an asymmetrical confluence when the main stream is dominant. In P. J. Ashworth, S. J. Bennet, J. L. Best, & S. J. McLelland (Eds.), *Coherent flow structures in open channels: Origins, scales, and interactions with sediment transport and bed morphology* (pp. 491–517). Wiley.
- Rhoads, B. L., & Johnson, K. K. (2018). Three-dimensional flow structure, morphodynamics, suspended sediment, and thermal mixing at an asymmetrical river confluence of a straight tributary and curving main channel. *Geomorphology*, 323, 51–69. <https://doi.org/10.1016/j.geomorph.2018.09.009>
- Rhoads, B. L., & Kenworthy, S. T. (1995). Flow structure at an asymmetrical stream confluence. *Geomorphology*, 11(4), 273–293. [https://doi.org/10.1016/0169-555x\(94\)00069-4](https://doi.org/10.1016/0169-555x(94)00069-4)
- Rhoads, B. L., & Kenworthy, S. T. (1998). Time-averaged flow structure in the central region of a stream confluence. *Earth Surface Processes and Landforms*, 23(2), 171–191. [https://doi.org/10.1002/\(sici\)1096-9837\(199802\)23:2<171::aid-esp842>3.0.co;2-t](https://doi.org/10.1002/(sici)1096-9837(199802)23:2<171::aid-esp842>3.0.co;2-t)
- Rhoads, B. L., & Kenworthy, S. T. (1999). On secondary circulation, helical motion and Rozovskii-based analysis of time-averaged two-dimensional velocity fields at confluences. *Earth Surface Processes and Landforms*, 24, 369–375. [https://doi.org/10.1002/\(sici\)1096-9837\(199904\)24:4<369::aid-esp983>3.0.co;2-f](https://doi.org/10.1002/(sici)1096-9837(199904)24:4<369::aid-esp983>3.0.co;2-f)
- Rhoads, B. L., & Sukhodolov, A. N. (2001). Field investigation of three-dimensional flow structure at stream confluences: 1. Thermal mixing and time-averaged velocities. *Water Resources Research*, 37(9), 2393–2410. <https://doi.org/10.1029/2001wr000316>
- Rhoads, B. L., & Sukhodolov, A. N. (2004). Spatial and temporal structure of shear layer turbulence at a stream confluence. *Water Resources Research*, 40, W06304. <https://doi.org/10.1029/2003WR002811>
- Rhoads, B. L., & Sukhodolov, A. N. (2008). Lateral momentum flux and the spatial evolution of flow within a confluence mixing interface. *Water Resources Research*, 44, W08440. <https://doi.org/10.1029/2007WR006634>
- Riley, J. D., Rhoads, B. L., Parsons, D. R., & Johnson, K. K. (2015). Influence of junction angle on three-dimensional flow structure and bed morphology at confluent meander bends during different hydrological conditions. *Earth Surface Processes and Landforms*, 40(2), 252–271. <https://doi.org/10.1002/esp.3624>
- Roy, A., & Bergeron, N. (1990). Flow and particle paths at a natural river confluence with coarse bed material. *Geomorphology*, 3(2), 99–112. [https://doi.org/10.1016/0169-555x\(90\)90039-5](https://doi.org/10.1016/0169-555x(90)90039-5)
- Rozovskii, I. L. (1954). Concerning the question of velocity distribution in stream bends. *DAN URSR Rep.*
- Rozovskii, I. L. (1957). *Flow of water in bends of open channels* (p. 233). Academy of Sciences of the Ukrainian SSR: Kiev (translated from Russian by the Israel Program for Scientific Translations).
- Rutherford, J. C. (1994). *River Mixing*. John Wiley & Sons.
- SonTek, Y. S. I. (2012). RiverSurveyor S5/M9 system manual firmware version 3.00.
- Stallard, R. F. (1987). Cross-channel mixing and its effect on sedimentation in the Orinoco River. *Water Resources Research*, 23(10), 1977–1986. <https://doi.org/10.1029/wr023i10p01977>
- Sukhodolov, A., & Sukhodolova, T. A. (2019). Dynamics of flow at concordant gravel river confluences: Effect of junction angle and momentum flux ratio. *Journal of Geophysical Research: Earth Surface*, 124, 588–615. <https://doi.org/10.1029/2018JF004648>

- Sukhodolov, A. N., Krick, J., Sukhodolova, T. A., Cheng, Z., Rhoads, B. L., & Constantinescu, G. S. (2017). Turbulent flow structure at a discordant river confluence: Asymmetric jet dynamics with implications for channel morphology. *Journal of Geophysical Research: Earth Surface*, *122*(6), 1278–1293. <https://doi.org/10.1002/2016JF004126>
- Szupiany, R. N., Amsler, M. L., Parsons, D. R., & Best, J. L. (2009). Morphology, flow structure, and suspended bed sediment transport at two large braid-bar confluences. *Water Resources Research*, *45*, W05415. <https://doi.org/10.1029/2008WR007428>
- Teledyne RD Instruments. (2013). WinRiver II software user's guide.
- Umar, M., Rhoads, B. L., & Greenberg, J. A. (2018). Use of multispectral satellite remote sensing to assess mixing of suspended sediment downstream of large river confluences. *Journal of Hydrology*, *556*, 325–338. <https://doi.org/10.1016/j.jhydrol.2017.11.026>
- Weber, L. J., Schumate, E. D., & Mawer, N. (2001). Experiments on flow at a 90 open-channel junction. *Journal of Hydraulic Engineering*, *127*(5), 340–350. [https://doi.org/10.1061/\(asce\)0733-9429\(2001\)127:5\(340\)](https://doi.org/10.1061/(asce)0733-9429(2001)127:5(340))
- Xu, X., Li, Y., Tan, Z., & Guo, Q. (2021). Groundwater, river water and lake water transformations in a typical wetland of Poyang Lake. *China Environmental Science*(04), 1824–1833. <https://doi.org/10.19674/j.cnki.issn1000-6923.2021.0194>
- Yuan, S., Tang, H., Li, K., Xu, L., Xiao, Y., Gualtieri, C., et al. (2021). Hydrodynamics, sediment transport and morphological features at the confluence between the Yangtze River and the Poyang lake. *Water Resources Research*, *57*(3). <https://doi.org/10.1029/2020WR028284>
- Yuan, S., Tang, H., Xiao, Y., Qiu, X., & Xia, Y. (2018). Water flow and sediment transport at open-channel confluences: An experimental study. *Journal of Hydraulic Research*, *56*, 333–350. <https://doi.org/10.1080/00221686.2017.1354932>
- Yuan, S., Tang, H., Xiao, Y., Qiu, X., Zhang, H., & Yu, D. (2016). Turbulent flow structure at a 90-degree open channel confluence: Accounting for the distortion of the shear layer. *Journal of Hydro-Environment Research*, *12*, 130–147. <https://doi.org/10.1016/j.jher.2016.05.006>
- Yuan, S., Xu, L., Tang, H., Xiao, Y., & Whittaker, C. (2022). Swimming behavior of juvenile silver carp near the separation zone of a channel confluence. *International Journal of Sediment Research*, *37*(1), 122–127. <https://doi.org/10.1016/j.ijsrc.2021.08.002>
- Yuan, S., Xu, L., Tang, H. W., Xiao, Y., & Gualtieri, C. (2022). The dynamics of river confluences and their effects on the ecology of aquatic environment: A review. *Journal of Hydrodynamics*, *34*, 1–14. <https://doi.org/10.1007/s42241-022-0001-z>
- Yuan, S., Zhu, Y., Tang, H., Xu, L., Li, K., Xiao, Y., & Gualtieri, C. (2022). Planform evolution and hydrodynamics near the multi-channel confluence between the Yarlung Zangbo River and the delta of the Niyang River. *Geomorphology*, *402*, 108157. <https://doi.org/10.1016/j.geomorph.2022.108157>
- Zhao, J., Chen, Z., & Zhang, H. (2014). A robust method for determining the heading misalignment angle of GPS compass in ADCP measurement. *Flow Measurement and Instrumentation*, *35*, 1–10. <https://doi.org/10.1016/j.flowmeasinst.2013.10.005>